Title

Cadherin-13 Maintains Retinotectal Synapses via Transneuronal Interactions

Journal

Journal of Neuroscience, 44(5)

ISSN

0270-6474

Authors

Matcham, Angela C
Toma, Kenichi
Tsai, Nicole Y
et al.

Publication Date

2024-01-31

DOI

10.1523/jneurosci.1310-23.2023

Development/Plasticity/Repair

Cadherin-13 Maintains Retinotectal Synapses via Transneuronal Interactions

Angela C. Matcham, Kenichi Toma, Nicole Y. Tsai, Christina J. Sze, Pin-Yeh Lin, Ilaria F. Stewart, and Xin Duan
Neuroscience Graduate Program, Department of Ophthalmology, Kavli Institute for Fundamental Neuroscience, University of California SanFrancisco, San Francisco 94143-2811, California

Maintaining precise synaptic contacts between neuronal partners is critical to ensure the proper functioning of the mammalian central nervous system (CNS). Diverse cell recognition molecules, such as classic cadherins (Cdhs), are part of the molecular machinery mediating synaptic choices during development and synaptic maintenance. Yet, the principles governing neuron–neuron wiring across diverse CNS neuron types remain largely unknown. The retinotectal synapses, connections from the retinal ganglion cells (RGCs) to the superior collicular (SC) neurons, offer an ideal experimental system to reveal molecular logic underlying synaptic choices and formation. This is due to the retina's unidirectional and laminar-restricted projections to the SC and the large databases of presynaptic RGC subtypes and postsynaptic SC neuronal types. Here, we focused on determining the role of Type II Cdhs in wiring the retinotectal synapses. We surveyed Cdhs expression patterns at neuronal resolution and revealed that Cdh13 is enriched in the wide-field neurons in the superficial SC (sSC). In either the Cdh13 null mutant or selective adult deletion within the wide-field neurons, there is a significant reduction of spine densities in the distal dendrites of these neurons in both sexes. Additionally, Cdh13 removal from presynaptic RGCs reduced dendritic spines in the postsynaptic wide-field neurons. Cdh13-expressing RGCs use differential mechanisms than αRGCs and On–Off Direction-Selective Ganglion Cells (ooDSGCs) to form specific retinotectal synapses. The results revealed a selective transneuronal interaction mediated by Cdh13 to maintain proper retinotectal synapses in vivo.

Key words: **cadherin; dendritic spine; neuron types; retinal ganglion cells; superior colliculus; synaptic choice**

Significance Statement

The Cadherin (Cdh) family of molecules is implicated in selective synaptic recognitions in intra-retinal circuits. However, their roles in wiring the rest of the central nervous system (CNS) remain undefined. The retinotectal synapses represent an established model for understanding selective neural circuit wiring between diverse presynaptic and postsynaptic neuron types. We first showed that Cdh13 is enriched in restricted superior colliculus neurons and allows cell type-specific spine maintenance from the retina to this population. These results show how differential Cdh expression can direct cell type-specific wiring beyond the retina into the rest of the mammalian CNS. The cellular and molecular mechanisms established in this study may further inform the understanding of Type II Cdh-related cognitive disorders.

Received July 8, 2023; revised Dec. 3, 2023; accepted Dec. 5, 2023.

Author contributions: A.C.M. and X.D. designed research; A.C.M., K.T., N.Y.T., C.J.S., P-Y.L., and I.F.S. performed research; K.T. and X.D. contributed unpublished reagents/analytic tools; A.C.M., C.J.S., I.F.S., and X.D. analyzed data; A.C.M. wrote the first draft of the paper; A.C.M., K.T., and X.D. edited the paper; X.D. wrote the paper.

We thank Y.N. Jan and L.Y. Jan for providing Leica SP8 for high-resolution imaging during the pandemic. We acknowledge E. Ullian, M. Parades, M. Scanziani, J. Horton, M. Feller, and J. Hyer for their advice. We thank Y.M. Kuo, S.Y. Chang, J. Palpant, M. Lum, and E. Dang for their technical support. We acknowledge NEI P30EY002162 for University of California San Francisco Vision Core support, the funding from the RPB unrestricted fund, and the RPB-CDA Awards to UCSF-Ophthalmology; from Whitehall Foundation Award, GRF-CFC3, and National Institutes of Health (NIH; R01EY030138; R01NS123912) to X.D.; NIH (F30EY033201) to N.Y.T.; and NIH (T32NS115706) to A.C.M.

The authors declare no competing financial interests.

Correspondence should be addressed to Xin Duan at xin.duan@ucsf.edu.

https://doi.org/10.1523/JNEUROSCI.1310-23.2023

Introduction

The precise assembly of neural circuits ensures accurate central nervous system (CNS) functions. This highly stereotypical process is achieved mainly developmentally. Visual circuits, for example, display prominent features of wiring specificity at each neuronal relay. Different subtypes of retinal ganglion cells (RGCs) extend long axons to a few major retinorecipient areas, including the superficial superior colliculus (sSC). RGC subtypes encode distinct visual features (Sanes and Masland, 2015) to distinguish lamina in the sSC and specific partners within the diversified population. Thus, synaptic choices in the retinotectal

system are a great model for understanding the molecular mechanisms underlying circuit wiring. Past studies using the retinotectal system have yielded significant insights into the cellular and molecular mechanisms regulating neurite outgrowth (Missaire and Hindges, 2015), axon guidance (Fredette et al., 1996; O'Leary and McLaughlin, 2005; Huberman et al., 2008), and molecular machinery for synapse formation (Ben Fredj et al., 2010; Cheng et al., 2010; Duan et al., 2018). However, the field is still waiting for an answer regarding how diverse RGC subtypes choose proper synaptic partners among different sSC neuron types, reflecting a general phenomenon in neural development termed synaptic specificity (Sanes and Yamagata, 2009; Duan et al., 2014; Yogev and Shen, 2014; Missaire and Hindges, 2015).

A leading hypothesis for synaptic specificity is for each neuronal subtype to possess a repertoire of cell surface recognition molecules directing the formation of specific synaptic contacts. It is hypothesized that these molecules mediate neuron–neuron interactions during development to stabilize synapses. The Cdh family of molecules is dynamically expressed among diversified neuron types and plays critical roles at multiple stages of neural development (Sanes and Yamagata, 2009; Hirano and Takeichi, 2012; Yogev and Shen, 2014). Cdhs localize in synaptic junctions (Yamagata et al., 1995; Fannon and Colman, 1996; Uchida et al., 1996; Benson and Tanaka, 1998; Huntley and Benson, 1999) and are necessary for various phases of long-term potentiation (Tang et al., 1998; Bozdagi et al., 2000; Manabe et al., 2000; Tanaka et al., 2000). Our past work focused on cell adhesion molecules, particularly Type II Cdhs in the inner retina circuits, to show that they instruct sublaminar axonal choices, dendritic arborization, and selected synapse formation in the retina (Duan et al., 2014, 2018; Yamagata et al., 2018; Graham and Duan, 2021). These findings were further validated in the assembly and function of hippocampal and spinal cord circuits (Basu et al., 2017; Dewitz et al., 2019; Vagnozzi et al., 2022).

We extended the study to retinotectal synapses to understand the role of Cdhs in synapse formation and maintenance. We focused on how Cdhs mediate the synaptic contacts from RGCs wiring to one of its major downstream targets, the superior colliculus (SC; Cang et al., 2018). Importantly, the retinotectal synapses offer a unique model, as these are critical steps in building precise visual circuits from the retina to the brain. Through expression pattern analysis at neuronal type resolution, we identified Cadherin-13 (Cdh13) as a candidate molecule to its observed unique enrichment in a singular neuronal SC population (named wide-field neurons.) Cdh13 was previously characterized as an exclusively homophilically binding protein, which was shown in synaptic modulation at different synapses (Ciatto et al., 2010; Killen et al., 2017; Kiser et al., 2019). To determine the potential role of Cdh13 in wide-field neuron wiring, we first focused on the dendritic spines. We examined their changes subject to Cdh13 null mutant or knockdown in the adult brain. When *Cdh13* is endogenously knocked out, mature wide-field neuron dendritic spines significantly decrease, with a disproportionate loss in the apical dendritic regions. This loss is similarly observed when Cdh13 is knocked down in the adult brain, strongly suggesting that it is necessary for mature spine maintenance in this population. In addition, given the homophilic role of Cdh13 in the CNS (Tanihara et al., 1994; Lehto and Sharom, 1998), we disrupted Cdh13 presynaptically in the retina. We examined the effects on postsynaptic dendritic spines in wide-fi eld neurons. Adult retinal Cdh13 elimination in RGCs locally decreased mature spine densities of the wide-field neurons in their axonal terminating areas. Additionally, we characterized that Cdh13-enriched RGCs were distinct from previously characterized αRGCs and On–Off Direction-Selective Ganglion Cells (ooDSGCs), thus representing a unique mechanism for selective synapse formation. These results indicate that Cdh13 is necessary for adult spine maintenance between RGCs and wide-field neurons. In summary, transneuronal Cdh13 from the retina to the brain is necessary to maintain mature dendritic spines in a cell type-specific manner. Understanding how specific Cdh13 expression directs cell type-specific wiring in the retinotectal projection not only expands our understanding of visual processing but may also expand our understanding of Cdh-directed CNS wiring as a whole.

Materials and Methods

Mice. All animal experiments were approved by the Institutional Animal Care and Use Committees at the University of California, San Francisco (UCSF). Mice were maintained under regular housing conditions with standard access to drink and food in a pathogen-free facility. Mice of both sexes were used in equal numbers, and no sexual dimorphisms were observed.

1. *Rorb*-Cre, *Ntsr1-GN209-Cre*, and *Grp-KH288-Cre* were previously used to label horizontal, stellate, wide-field, and narrow-field neurons in the SC (Gale and Murphy, 2018). *Ntsr1-GN209-Cre* and *Grp-KH288-Cre* were generous gifts of Charles Gerfen (National Institute of Mental Health).
2. *Cdh13-CreER* knock-in line was a generous gift of Joshua Sanes (Harvard University). The knock-in line has $CreER^{T2}$ replacing the first coding exon of *Cdh13* transcript as previously characterized (Poliak et al., 2016). Tamoxifen was injected intraperitoneally (2 mg per dose) for three doses to induce CreER activities in adult animals.
3. *vGlut2-Cre* (JAX: 016963) were previously characterized to label all RGCs in both development and adult eyes (Tran et al., 2019).
4. *Thy1-LoxP-Stop-LoxP-YFP* reporter line #15 (*Thy1-LSL-YFP*) was a generous gift from Joshua Sanes (Harvard University). The transgenic mice express EYFP driven by Cre recombinase in neuronal populations, including most RGCs and projection neurons in the retina, brain, and spinal cord. To visualize neuronal morphology, we crossed this line with the SC neuron-marking Cre driver lines and the *Cdh13-CreER* line listed above (Buffelli et al., 2003).

Neonatal transcranial injections. Neonatal superior collicular injections were performed on postnatal day (P) 0/1 when the lambdoid suture and collicular hemispheres were still visible through the skin. The mouse is anesthetized on ice in accordance with protocols. The viral infection is made with a pulled glass pipette through the skin and the skull (volume 0.33 µl per hemisphere). Control shRNA virus was injected in littermates as the control. The mouse was returned to the cage after being warmed and alert.

Adult stereotaxic injections. Mice were anesthetized with continuous 2% isoflurane/oxygen on a stereotaxic setup (model 940, David Kopf Instruments). Meloxicam (5 mg/kg) was administered intraperitoneally before the surgery and 1 d after surgery. Viruses were loaded into a pulled glass pipette connected with a syringe (7634-O, Hamilton) by a dual ferrule adaptor (55750-0, Hamilton). Injection speed and volume were controlled by a Microinjection Syringe pump (UMP3T-1, World Precision Instruments). AAV-U6-sh*Cdh13-Ef1a-DIO-mOrange2* was injected into the right hemisphere of P60 *Ntsr1-GN209-Cre* mice. Coordinates were as follows: 3.6 mm posterior, 0.7 mm lateral to bregma, and 1.0 mm below the skull. Volume was 300 nl. Four weeks later, the mouse was humanely killed via transcardial perfusion (see histology). Brain and retinas were collected for immunohistochemical analysis.

Intraocular injections. Intraocular injection of adeno-associated virus (AAVs) was performed as previously described (Hong et al., 2011; Duan et al., 2015): For the Cdh13-RGC axonal tracing experiment, p1 *Cdh13-CreER* mice were injected uni-ocularly with 0.5 µl AAV-*DIO-GFP* using a sharpened glass pipette. For the retinal Cdh13 knockdown experiment, P60 *Ntsr1-GN209-Cre* was injected with 1 µl AAV-U6-sh*Cdh13-Ef1a-DIO-mOrange*2 or control AAVs in the right eye.

Eye enucleation experiments. Unilateral eye enucleation experiments were carried out as previously described (Kim et al., 2010). In brief, adult animals were anesthetized under 2% isoflurane/oxygen. Meloxicam (5 mg/kg) was administered intraperitoneally before the surgery and 1 d after surgery. Curved scissors were used to sever optic muscles and optic nerves to remove the eye with minimal bleeding and internal trauma. Animals were monitored for distress and pain every day for 5 d post-surgery.

Adeno-associated virus production. AAV2 (Serotype 2) production protocol was carried out as previously described (Duan et al., 2015). To make pAAV-hU6-sh*Cdh13-Ef1a-DIO-mOrange2* for Cdh13 LOF studies, we inserted hU6-shCdh13 cassettes into pAAV-Ef1a-DIO-mOrange2, a backbone of shRNA plasmid, which was modified from pAAV-Ef1a-DIO-ChR2-EYFP (Addgene #35507), replacing the ChR2-EYRP to mOrange2. The target sequences were adopted from (Killen et al., 2017) and validated. shCdh13#1: 5′-GCAACGAGAAGCTGCACTA; shCdh13#2: 5′-GCTCCTTGCAGGATATCTT; control shRNA-sequence was adopted from (Duan et al., 2007): AGTTCCAGTACGGCTCCAA.

Immunohistochemistry. Animals were anesthetized and then transcardially perfused with ice-cold 0.1 M phosphate buffer, then ice-cold 4% PFA in 0.1 M phosphate buffer, pH 7.4. The whole brain and eyes were collected where applicable. Dissected brain tissue was then post-fixed in the PFA solution overnight at 4°C and then cryoprotected in 30% sucrose and 0.2% sodium azide until they sank. The brain samples have the option to be stored at this step. Dissected eyes were placed in 4% PFA for 30 min on ice. The cornea and lens were then removed before a second 30 min incubation period in 4% PFA on ice. After sucrose cryoprotection, brains were frozen with dry ice on a sliding microtome (Leica). Floating 40 µm sections were collected and stored in 0.1 M PBS with 0.2% sodium azide at 4°C. These sections underwent immunohistochemical staining, in situ hybridization staining, or both. For immunostaining, floating sections were incubated in blocking buffer (0.5% Triton X-100, 5% natural donkey serum, 0.1 M PBS) at room temperature (RT) for 1 h, then primary antibodies in blocking buffer overnight at 4°C, and then secondary antibodies in blocking buffer at RT for 2 h.

In situ hybridization was performed using RNAscope Multiplex Fluorescent V2 Kit (Advanced Cell Diagnostics) following the manufacturer's instructions. The following ACDBio RNAscope probes were applied: Mm-Cdh13-C1 (ACD-Bio catalog #443251); Npnt-C2 (ACD-Bio catalog #316771); Etv1-C3 (ACD-Bio catalog #557891); and RFP-C3 (ACD-Bio catalog #464341). Floating 40 µm sections were mounted on polarized glass slides for this protocol. Where applicable, samples were then immunostained using the protocol previously.

Retinas were dissected from the remaining eye sample stored in 0.1 M PBS, 0.2% sodium azide. For whole-mount immunohistochemistry, the retina is incubated in a blocking buffer overnight at 4°C. The sample is incubated in a blocking buffer for three nights in 4°C in primary antibodies. After washing in 0.1 M PBS, the sample is incubated overnight at 4°C in secondary antibodies in a blocking buffer. The sample is then washed in PBS before mounting on filter paper and Vectashield with DAPI (VectorLabs H-1200) and covered with glass slips. Retinas for slice immunostaining or in situ hybridization were cryoprotected in 30% sucrose for 60 min on ice or until it sinks. It is then frozen in OCT (Tissue-Tek) in a block. The sample is cryostat sectioned at 20 µm and directly mounted on polarized glass slides. Mounted tissue was either stored at −20°C or directly stained. Primary antibodies used for the SC stain included rabbit anti-GFP (1:1,000, Life Technologies), rabbit anti-RFP (1:1,000, Rockland), rat anti-MBP (1:500, Abcam), goat anti-vAChT (1:500, Promega), rabbit anti-Pvalb (1:5,000, PV27 Swant), rabbit anti-calbindin (1:10,000, Swant), and rabbit anti-Calretinin (1:5,000, Millipore). Primary antibodies used for the retina stain included mouse anti-NeuN (1:500, Millipore), chicken anti-GFP (1:1,000, Abcam), rabbit anti-Foxp2 (1:1,000, Abcam), rabbit anti-Melanopsin (1:500, Advanced Targeting Systems), and rabbit anti-Tbr1 (1:500, Cell Signaling), guinea-pig anti-RBPMS (1:1,000, PhosphoSolutions); and goat anti-Osteopontin/Spp1 (1:500, R&D Systems). Secondary antibodies were conjugated to Alexa Fluor 488, Alexa Fluor 568, or Alexa Fluor 647 (Jackson ImmunoResearch) and used at 1:500.

Quantification and statistical analysis. Confocal images were acquired using a Leica SP8 confocal microscope (Leica Microsystems) and Zeiss LSM900 (Carl Zeiss Microscopy). For superior colliculus sections, sections were coronally sliced at 40 µm and sampled in 280 µm intervals from the posterior to the anterior superior colliculus. The 10× images to establish laminar boundary staining (MBP and vAChT) were taken on a Leica SP8. All cells/dendrites, medial-laterally, were analyzed within each coronal section. Images taken for dendritic spine analysis were taken with a Zeiss LSM900 to ensure sufficient image resolution. Images were analyzed using ImageJ software (NIH). Only contrast and brightness were adjusted for all images consistently between samples. ImageJ simple neurite tracer was used to isolate dendrites and analyze spine type and length.

ImageJ was used to process all images. GraphPad Prism 9/10 was used to generate graphs and statistical analyses. Statistical methods and the number of animals tested with each configuration are presented in the legend for each figure. For comparisons between the two groups, a Kolmogorov–Smirnov test was performed. *D*-values and p values are reported. For the statistical analysis of multiple groups, a Kruskal–Wallis test was performed. Kruskal–Wallis values and p values are reported. When the Kruskal–Wallis test is significant, subsequent Kolmogorov–Smirnov tests are conducted. Statistical significance was defined as ns, not significant, $^{*}p < 0.05$, $^{**}p < 0.01$, $^{***}p < 0.001$, and $^{****}p < 0.0001$. All data are presented as means ± SEM unless stated otherwise.

1. To quantify the protein expression of *Ntsr1-GN209-Cre* labeled SC cells: *Ntsr1-GN209-Cre; Thy1-LSL-YFP* coronal brain sections were stained for the target protein or mRNA and GFP. Co-expression was determined using ImageJ to determine the overlap of the target protein and the GFP marking the *Ntsr1-GN209-Cre* cells.
2. To quantify spine density, target SC cells were isolated via controlled tamoxifen administration in *Cdh13-CreER; Thy1-LSL-YFP*, or low titer viral injection. High-resolution 63× images taken on the Zeiss LSM900 along the dendrites of an isolated cell to visualize dendritic spines. These spines were analyzed using ImageJ simple neurite tracer. The dorsal–ventral location of the spines was determined in relation to a 10× image of the same neuron, taken as a "map" for the dendritic spine locations. Further description of the dorsal–ventral location designation is described in Figure 3*E*. Only dendrites attached to *Cdh13-CreER; Thy1-LSL-YFP* labeled cell bodied in the SO with wide-field neuron cell body morphology were analyzed.
3. To quantify knockdown efficiency after AAV-U6-sh*Cdh13-Ef1a-DIO-mOrange2*, co-expression of mOrange2 mRNA expression labeled by RFP mRNA probe and Cdh13 mRNA (stained via RNAScope) was determined in both the SC and the retina. The 40 µm SC slices were stained using RNAScope and imaged using a Leica SP8 at 40× in 1 µm z-step intervals. The 20 µm retina slices of the same animal was stained and imaged in the same manner and batch. Co-expression was determined using ImageJ.
4. To determine the axonal termination zones of retinal Cdh13-knockdown RGCs, we artificially drawn three-dimensional polygons around the RFP-labeled RGC axons in 40 µm SC brain slices. GFP antibody amplified *Cdh13-CreER; Thy1-LSL-YFP* dendrites were

analyzed in a consistent manner with previous experiments, but spines and their densities were categorized based on their location within or outside of the polygon.

Results

Cdh13 is uniquely enriched in wide-field neurons in the superior colliculus

We first surveyed Cdh expression patterns in the sSC using genetic marking lines for Cdh-expressing neurons at high precision (Duan et al., 2014, 2018). In addition, we also aligned Cdh-expressing neuron populations to the established sSC marking lines, primarily via a screen of BAC transgenic mouse collection (Gale and Murphy, 2014, 2018). This strategy allowed us to efficiently register Cdh expressions onto corresponding neuron subpopulations in the sSC. It was also important to consistently identify sSC laminar boundaries and each neuronal population about them. To do this, we visualized laminar boundaries by staining for two established molecular markers (Fig. 1*A*): the boundary between the stratum griseum superficiale (SGS) and stratum opticum (SO) is visualized by Myelin Binding Protein (MBP) staining; the lower SO boundary is visualized by Vesicular Acetylcholine Transporter protein (vAChT) staining (Byun et al., 2016). The boundaries established by these two markers enable us to register Cdh expression patterns onto morphological cell types efficiently. For this study, all SC images are oriented with the lateral side on the left and the medial side on the right.

We focused on three excitatory types of SC neurons based on morphometric standards that are highly stereotypical: stellate neurons, narrow-field neurons, and wide-field neurons corresponding to neurons marked in three distinct transgenic mouse lines, *Rorb-Cre*, *Grp-KP288-Cre*, and *Ntsr1-GN209-Cre*, respectively (Gale and Murphy, 2014). A genetic cross to Thy1-LoxP-Stop-LoxP-YFP reporter line (Thy1-LSL-YFP; Buffelli et al., 2003; Fig. 1*B*,*C*) further demonstrated their laminar distribution: *Rorb-Cre*-positive stellate neurons, as well as possible Horizontal cells (Oliveira and Yonehara, 2018), were restricted to the SGS; *Grp-KP288-Cre* narrow-field neurons resided within the SO along the SGS and SO boundary; and *Ntsr1-GN209-Cre* wide-field neurons have cell bodies in the lower SO with large, complex, dendritic arbors that reach to the upper SGS.

In parallel to the BAC transgenics listed above, we established a set of Cdh-marking lines via knock-in to visualize specific Cdh-expressing neurons throughout the nervous system (Suzuki et al., 2007; Poliak et al., 2016; Duan et al., 2018). Such a genetic system allows us to mark the neurons with detailed neuronal morphology using either LacZ labeling or a Cre-dependent marking system. Based on a survey of Cdhs expression in the Allen Institute Brain Atlas, we focused on Cdhs with subset expression in the superficial SC and assessed Cdh4-, Cdh8-, or Cdh13-expressing neurons (Fig. 1*D*).

Notably, Cdh13-expressing SC neurons share similar morphological and laminar similarity to wide-field neurons marked by *Ntsr1-GN209-Cre* lines. We then established a *Cdh13-CreER; Thy1-LSL-YFP* cross, to visualize these neurons in the superficial SC. Cdh13-SC neurons exhibited large soma in the lower SO with large, complex dendritic arbors reaching the surface of the SGS (Fig. 1*D*), as those neurons characterized in the *Ntsr1-GN209-Cre* line (Fig. 1*B*,*C*). To cross-register the *Cdh13-CreER* line and *Ntsr1-GN209-Cre* line for wide-field neuron marking, we carried out in situ hybridization of Cdh13 onto *Ntsr1-GN209-Cre*; *Thy1-LSL-YFP* neurons and showed that 91.8 ± 2.3% (mean ± SEM; $n = 5$ mice) of total Ntsr1-SC neurons express Cdh13 (Fig. 2*E*,*F*). In contrast, Cdh13 expression is absent in *Rorb-Cre* stellate cells and *Grp-KP288-Cre* narrow-field cells (Fig. 2*A*–*D*,*J*) ($n = 5$ mice each). This observation corroborated our recent single-cell RNA-seq data showing that, among three corresponding excitatory cell clusters in the sSC, only one has enriched Cdh13 expression in the corresponding Npnt-positive wide-field neuron cluster (Fig. 2*I*; Tsai et al., 2022). Additionally, we showed that wide-field neurons were not marked by several previously characterized markers in the sSC, such as parvalbumin, calbindin, and calretinin through immunohistochemistry or *Etv1* through in situ hybridization (Fig. 2*G*,*H*). Notably, 86.56 ± 2.99% (mean ± SEM; $n = 5$ mice) of these wide-field neurons express Npnt mRNA (Fig. 2*H*), previously characterized as an extracellular matrix molecule enriched in wide-field neurons (Tsai et al., 2022). *Ntsr1-GN209-Cre* line marks wide-field neurons via positioning effects, while the *Ntsr1* transcript is absent in the sSC (Tsai et al., 2022). In contrast, Cdh13 serves as an endogenous marker for wide-field neurons. Notably, there are 35.7 ± 1.7% (mean ± SEM; $n = 3$ mice) Cdh13-expressing wide-field neurons in the SO that are not labeled in the *Ntsr1-GN209-Cre* line (Fig. 2*F*,*K*). We therefore use *Cdh13-CreER* marking lines to study wide-field neurons in the sSC.

Cdh13 knock-outs lead to a reduction of mature spines in wide-field neuron apical dendrites

The *Cdh13-CreER* mouse line has the $CreER^{T2}$ knocked in to disrupt the first coding exon of *Cdh13* (Poliak et al., 2016). Thus, homozygotes of the *Cdh13-CreER* allele led to a *Cdh13 null* (Fig. 3*A*). This also results in consistently labeling the Cdh13 population in the heterozygous (control) and homozygous (knock-out) mice, respectively. We confirmed the *Cdh13* knock-out in the homozygotes with complete loss of Cdh13 expression (Fig. 3*B*). As a control, we showed that Npnt staining, another marker for wide-field neurons (Tsai et al., 2022), is not perturbed in terms of neuron densities or laminar location between *Cdh13* knock-out and heterozygotic controls (Fig. 3*B*, green). The heterozygous mouse has one functional *Cdh13* allele and, therefore, robustly expresses *Cdh13* mRNA (Fig. 3*B*, red) that co-expresses (Fig. 3*B*, yellow) with wide-field neuron bodies, labeled with Npnt (Fig. 3*B*, green). We further found that one copy of Cdh13 in the heterozygous *Cdh13-CreER* mice was sufficient to maintain synaptic structures when compared with wide-field neurons labeled in *Ntsr1-GN209-Cre* line in terms of total spine numbers and spine distribution along the dendrite (Fig. 3*C*,*D*,*F*). *Ntsr1-GN209-Cre* neurons had a spine density of 93.6 ± 8.5 spines/mm (mean ± SEM), while heterozygous Cdh13-positive wide-field neurons had a similar spine density at 98.8 ± 7.1 spines/mm (mean ± SEM; Kolmogorov–Smirnov $D = 0.16$; $p = 0.78$; $n = 150$ dendrites). In addition, no difference in spine distribution was observed (proximal: Kolmogorov–Smirnov $D = 0.24$, $p = 0.61$; medial: Kolmogorov–Smirnov $D = 0.31$, $p = 0.46$; apical Kolmogorov–Smirnov $D = 0.22$, $p = 0.86$; Fig. 3*C*). Therefore, heterozygous littermates are used as the control compared with homozygous littermates.

Using this transgenic system, we analyzed the spine densities of the heterozygous control and homozygous *Cdh13* knock-out wide-field neurons in the SC. Notably, a significant decrease in the number of spines per unit length of dendrite was observed in *Cdh13* homozygote knock-outs (39.3 ± 5.1 spines/mm; mean ± SEM) compared with control spine densities (98.8 ± 7.0 spines/mm; mean ± SEM; Fig. 4*A*,*B*). Classically, there are four

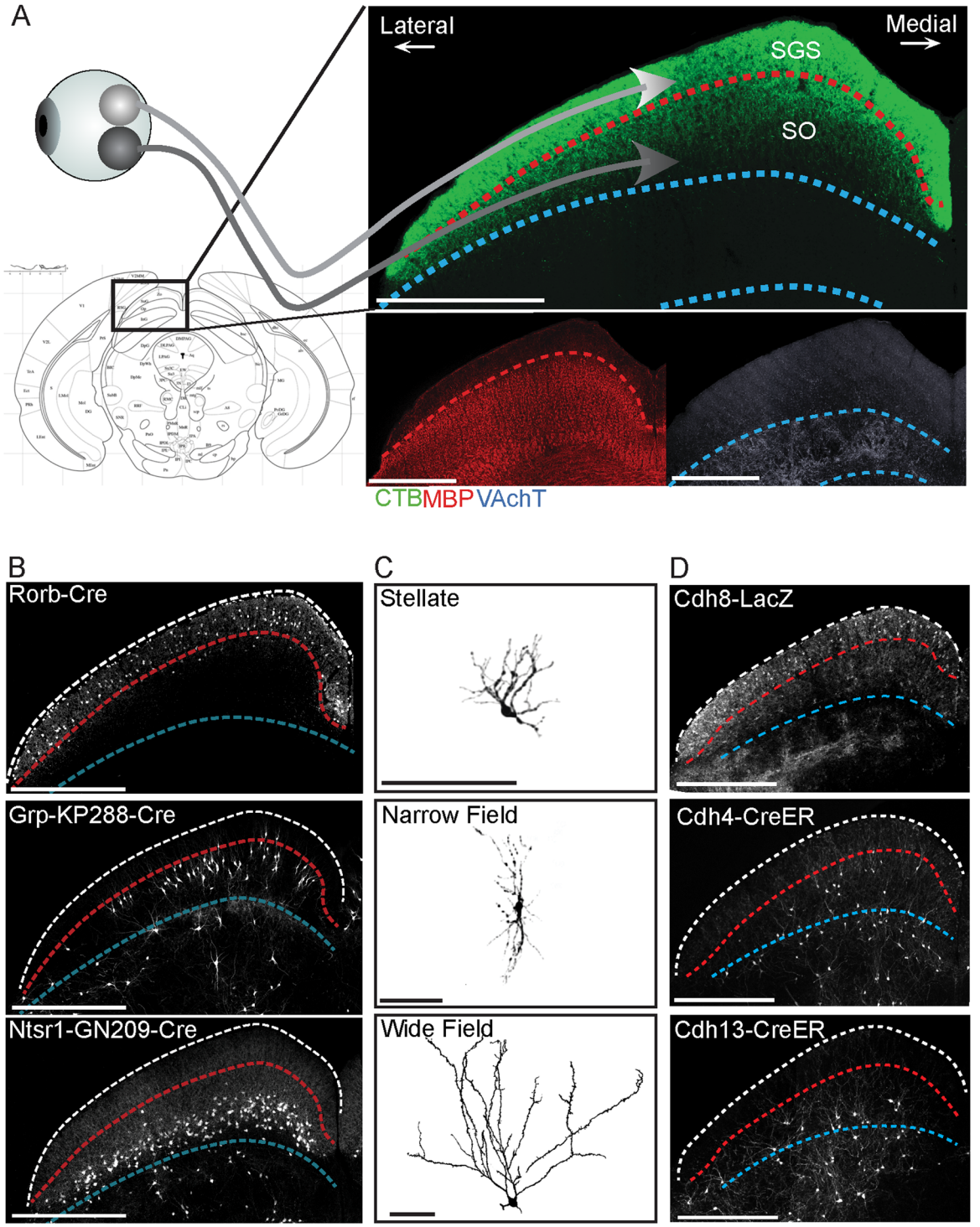

Figure 1. BAC transgenic labeled and cadherin-marking line comparison in the SC. ***A***, Schematic of superior colliculus lamination visualized using immunostaining and RGC axonal input (green) labeled by cholera toxin B conjugated to 488 nm fluorescent protein. MBP (red) and vAChT (blue) immunostains label the lower boundaries of the SGS and SO, respectively. SC laminar boundaries will be defined as these colors for the duration of the study, and all example images were taken between −3.5 to −4.0 mm bregma. ***B***, Confocal images of coronal slices of superior colliculi of BAC transgenic mice label specific SC cell types. Stellate cells are labeled by *Rorb-Cre*, narrow-field cells are labeled by *Grp-KP288-Cre*, and wide-field cells are labeled by *Ntsr1-GN209-Cre*. The laminar location of each population is shown compared with MBP (red) and vAChT (blue) boundaries. ***C***, Isolated representative neurons taken from transgenic mouse lines presented in ***B***. Neurons were isolated using the ImageJ neurite tracer. ***D***, Confocal images of coronal slices of superior colliculi of transgenic mice labeling Cdh-expressing cells. Cdh8 is labeled by the *Cdh8-LacZ* mouse line. Cdh4 and Cdh13 are labeled by Cre-ER with Thy1-LSL-YFP-15. The laminar location of each population is shown compared with MBP (red) and vAChT (blue) boundaries and is comparable with those in ***B***.

major spine types: stubby, narrow, mushroom, and filopodia, all of which are observed on wide-field neuron spine dendrites (Molenaar, 1992; Zito and Svoboda, 2002; Hayashi and Majewska, 2005; Zhao et al., 2006; Fig. 4*C*). Mushroom spines are considered mature spines and are associated with housing a functional postsynaptic density. They are defined by having a

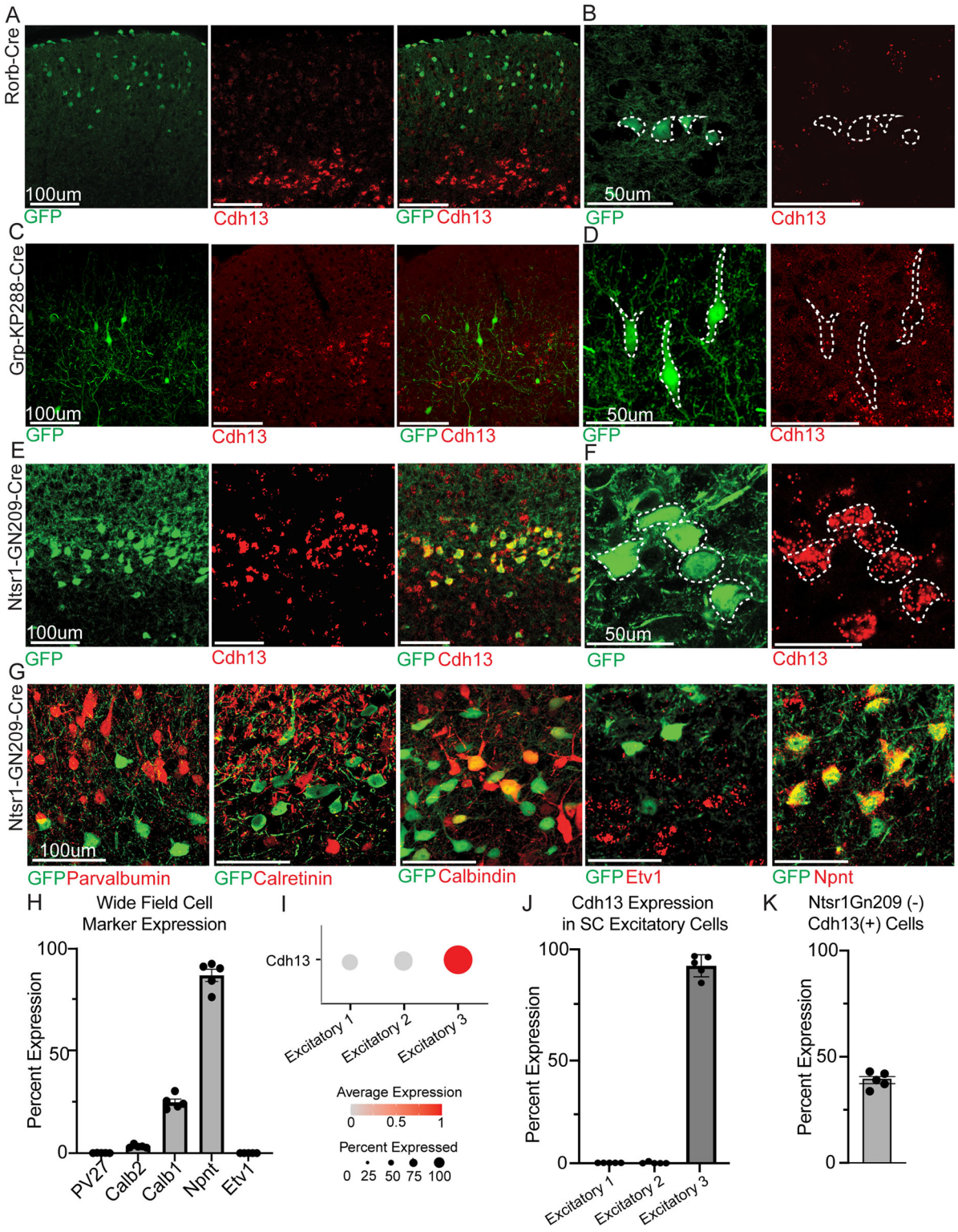

Figure 2. Cdh13 expression in superior colliculus excitatory neurons. ***A***, Confocal images of *Rorb-Cre; Thy1-LSL-YFP15* cells in the SC (green) compared with *Cdh13* mRNA expression (red). ***B***, Zoomed in confocal images of *Rorb-Cre; Thy1-LSL-YFP15* cells in the SC (green) compared with *Cdh13* mRNA expression (red). The white dotted line indicates stellate cell body boundaries. ***C***, Confocal images of *Grp-KP288-Cre; Thy1-LSL-YFP15* cells in the SC (green) compared with *Cdh13* mRNA expression (red). ***D***, Zoomed in confocal images of *Grp-KP288-Cre; Thy1-LSL-YFP15* cells in the SC (green) compared with Cdh13 mRNA expression (red). The white dotted line indicates stellate cell body boundaries. ***E***, Confocal images of *Ntsr1-Gn209-Cre; Thy1-LSL-YFP15* cells in the SC (green) compared with Cdh13 mRNA expression (red). ***F***, Zoomed in confocal images of *Ntsr1-Gn209-Cre; Thy1-LSL-YFP15* cells in the SC (green) compared with Cdh13 mRNA expression (red). The white dotted line indicates stellate cell body boundaries. ***G***, Molecular expression in *Ntsr1-Gn209-Cre; Thy1-LSL-YFP15* labeled wide-field cells example images. Pvalb, Calb1 (calbindin), and Calb2 (calretinin) are immunohistochemical stains, while Etv1 and Npnt are stained using in situ hybridization. ***H***, Quantifications of *Ntsr1-GN209-Cre; Thy1-LSL-YFP15* cell expression. 0.11 ± 0.02% express Pvalb, 24.8 ± 1.5% express Calb1, 3.5 ± 0.4% express Calb2, 0.00 ± 0.00% express Etv1, 86.56 ± 2.99% express Npnt. $n = 5$ mice. ***I***, Single-cell RNA-Seq for all retinorecipient excitatory neurons, showing enriched expression of Cdh13 in only one cluster of excitatory cells (Npnt-positive wide-field neurons). ***J***, Quantifications of Cdh13 expression in stellate (0.00% $n = 5$ mice), narrow-field (0.00% $n = 5$ mice), and wide-field cells (91.8 ± 2.3% $n = 5$ mice). ***K***, Quantifications of Cdh13-enriched wide-field neuron cell bodies that are not represented in the *Ntsr1-GN209-Cre; Thy1-LSL-YFP15* population (35.7 ± 1.7%).

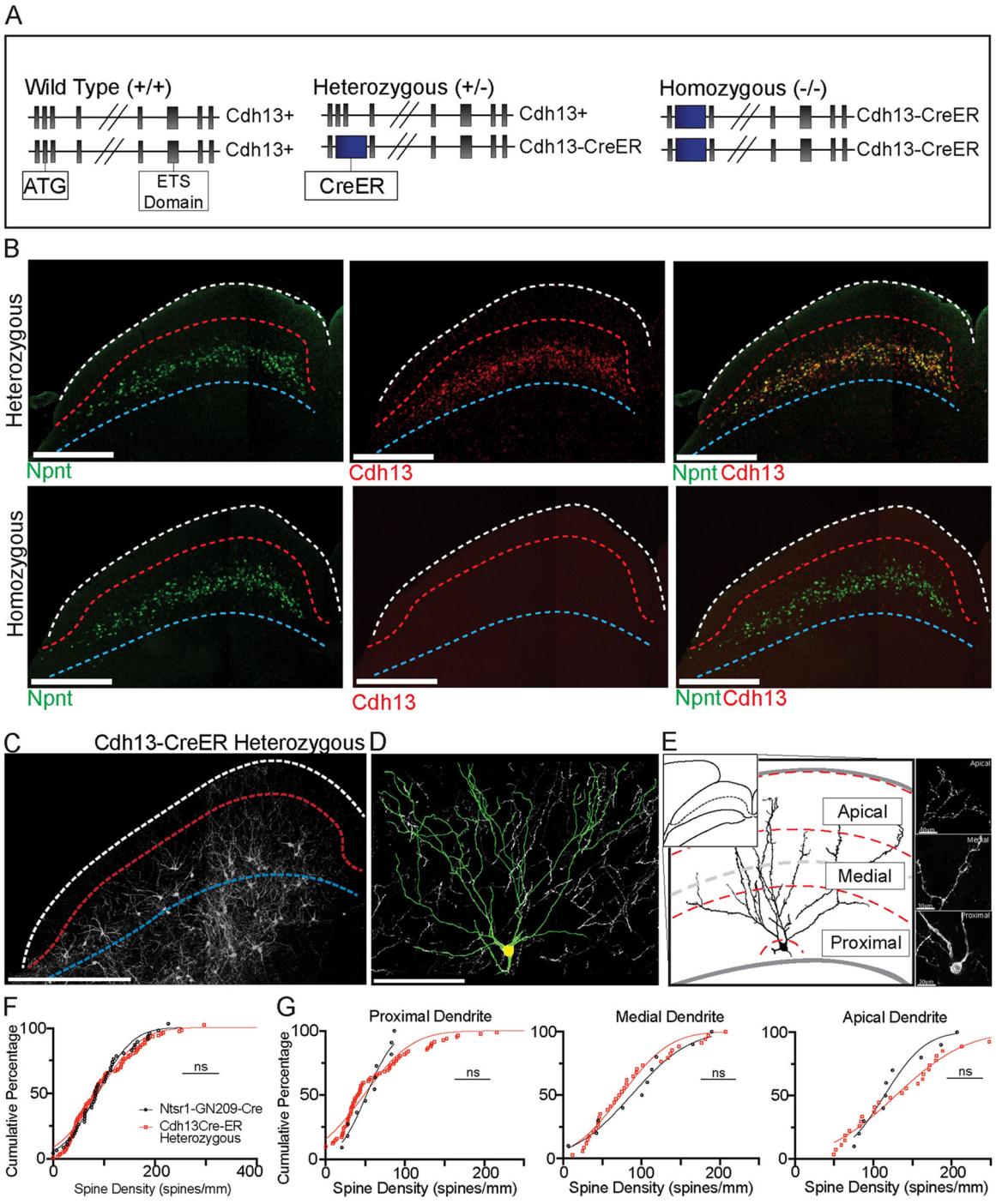

Figure 3. Homozygous *Cdh13-CreER* transgenic mice labels Cdh13-expressing cells while knocking out Cdh13 expression. ***A***, Genetic layout of *Cdh13-CreER* mice. The *CreER* region is knocked into the transcription initiation region of the *Cdh13*-gene, knocking out functional *Cdh13* transcription. The heterozygous mouse (middle) has one functional copy of the *Cdh13* gene, while a homozygous mouse (right) has a complete knock-out of *Cdh13* expression. ***B***, Top, *Cdh13-CreER* heterozygous mice continue to express *Cdh13* mRNA in the appropriate lamina in wide-field neurons. Wide-field neurons are labeled by Npnt mRNA (green, left) with co-expression with *Cdh13* mRNA (red, center). Bottom, Confirmation of knock-out in the homozygous but not heterozygous mice while maintaining wide-field neuron laminar location and density. *Npnt* mRNA (green, left) lamination and density are maintained, while *Cdh13* mRNA (red, center) is abolished with no co-expression (yellow, right). $n = 5$ mice. ***C***, Confocal image of *Cdh13-CreER* mouse line labeled neurons. Labeled Cdh13 cell bodies are laminarly restricted to the lower SO, like *Ntsr1-GN209* wide-field neurons. Scale bar, 500 µm. ***D***, Isolated *Cdh13-CreER* labeled cells have wide-field neuron morphology. Scale bar, 125 µm. ***E***, Diagram depicting proximal, medial, and apical dendrite boundaries. Boundaries are determined in a Sholl-like analysis determined by the location of the cell body and surface of the SC surface, divided into three equal sections. ***F***, Cumulative percent graph comparing dendritic spine density between *Cdh13-CreER* Het labeled cells and *Ntsr1-GN209* labeled cells. There is no significant difference (Kolmogorov–Smirnov $D = 0.16$; $p = 0.78$; $n = 150$ dendrites). ***G***, Cumulative percent graphs comparing spine density distribution along the dendrite. Spine distribution between *Cdh13-CreER* cells and *Ntsr1-GN209-Cre* is not significantly different at all locations (proximal: Kolmogorov–Smirnov $D = 0.24$, $p = 0.61$; medial: Kolmogorov–Smirnov $D = 0.31$, $p = 0.46$; apical: Kolmogorov–Smirnov $D = 0.22$, $p = 0.86$).

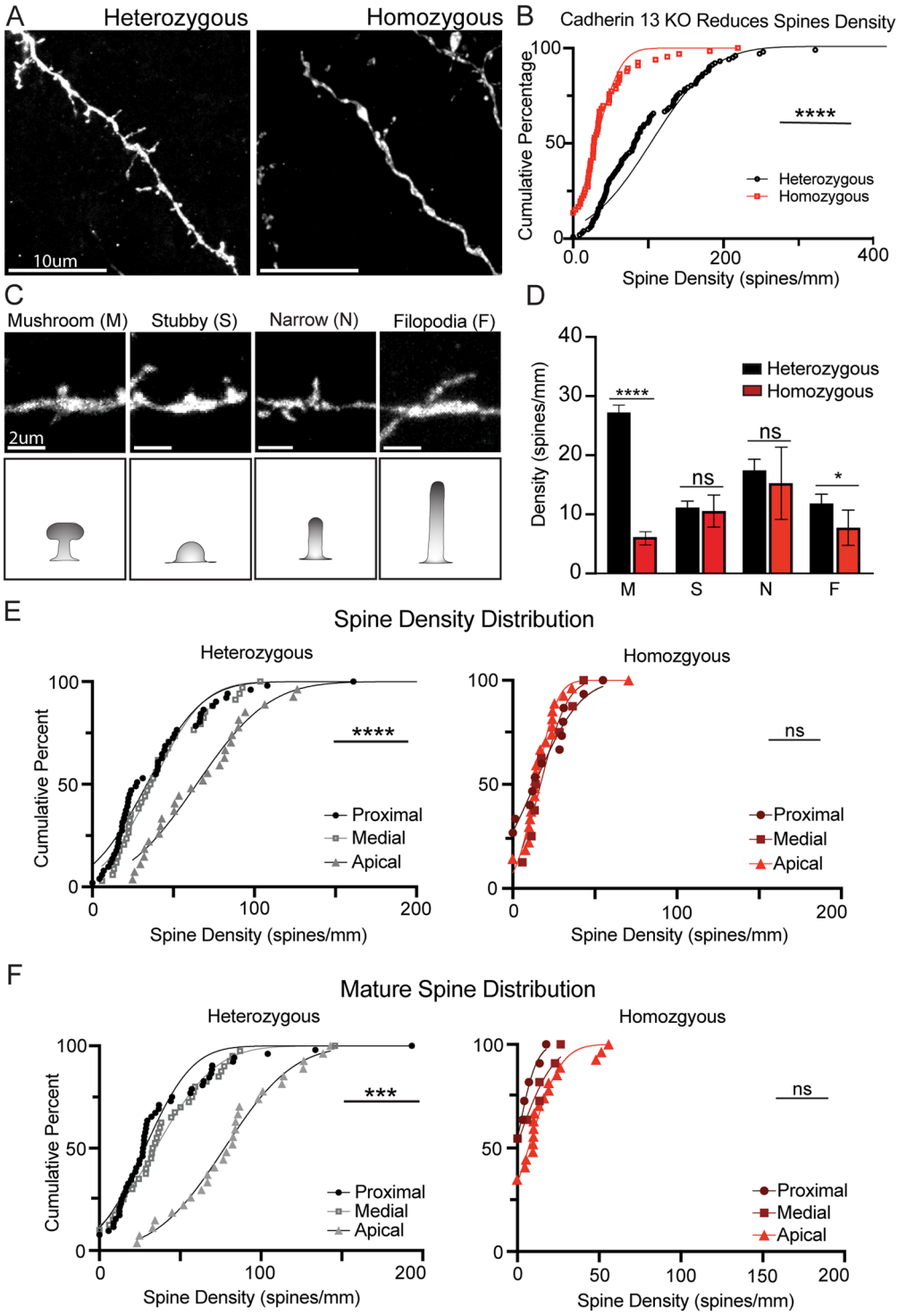

Figure 4. *Cdh13* knock-outs lead to reduced mature spines in wide-field neuron dendrites. ***A***, Dendritic spines are visible in both *Cdh13-CreER* heterozygous (left) and homozygous (right), with a decrease in the number of spines in the homozygous knock-out condition. Scale bar, 10 µm. ***B***, Cumulative percent distribution of dendritic spine density is significantly reduced when *Cdh13* is endogenously knocked out compared with the heterozygous control (Kolmogorov–Smirnov $D = 0.51$; $p < 0.0001$; $n = 168$ dendrites). ***C***, Four spine morphologies are observed in our *Cdh13-CreER; Thy1-Stp-YFP15* mice. Top, Example images of spines from heterozygous mice. Each spine type was also observed in homozygous samples (data not shown). Scale bar, 2 µm. ***D***, Comparisons of densities of each spine morphology show a significant decrease in mushroom (Kolmogorov–Smirnov $D = 0.37$; $p < 0.0001$) populations but not in stubby (Kolmogorov–Smirnov $D = 0.16$; $p = 0.30$), narrow (Kolmogorov–Smirnov $D = 0.18$; $p = 0.28$), or filopodia (Kolmogorov–Smirnov $D = 0.23$; $p = 0.03$); $n = 5$ animals per condition; 158 dendrites per condition. ***E***, Comparison of cumulative percent distributions of overall spine densities at different locations along the dendrite from the cell body show a disproportionate decrease of spines in the apical regions in the knock-out (right; reds; Kruskal–Wallis = 2.49; $p = 0.29$; $n = 49$ dendrites) compared with the control (left; blacks; Kruskal–Wallis = 28.87; $p < 0.0001$; $n = 119$ dendrites). ***F***, The disproportionate decrease in the apical regions is observed in mature spine distributions in knock-out conditions (right; reds; Kruskal–Wallis = 1.03, $p = 0.60$; $n = 49$ dendrites) compared with the control (left; blacks; Kruskal–Wallis = 17.18, $p = 0.0002$; $n = 119$ dendrites). $n = 5$ mice per condition. Each data point represents a dendrite. ns, $p > 0.05$, *$p < 0.05$, **$p < 0.01$, ***$p < 0.001$, ****$p < 0.0001$.

head larger than the neck of the spine. All spine types were observed in both knock-out and control samples. This shows that transgenic fluorescent labeling is sufficient for labeling all spines in both conditions. Looking at density changes of each spine type, we observed significant decreases in mature mushroom spine density: 9.6 ± 1.9 spines/mm (mean ± SEM) versus 47.5 ± 3.4 spines/mm (mean ± SEM; Fig. 4*D*). No significant change in narrow, stubby, or filopodia densities is observed [stubby (Kolmogorov–Smirnov $D = 0.16$; $p = 0.30$), narrow (Kolmogorov–Smirnov $D = 0.18$; $p = 0.28$), or filopodia (Kolmogorov–Smirnov $D = 0.23$; $p = 0.03$); $n = 5$ animals per condition; 158 dendrites per condition; Fig. 4*D*].

Because sSC neurons and their inputs are highly laminarly organized, we examined whether Cdh13-dependent changes to mature spines are restricted to specific lamina. To test this, we divided dendritic arbors into three zones according to their morphology and distance to the SC surface. The proximal region consists of thick primary dendrites in the lower one-third, between the cell body and the surface of the SC. The apical region consists of thin, complex dendritic terminations in the upper one-third between the cell body and the SC surface. At the same time, the medial region is one-third, between the proximal and apical regions consisting of "classical" dendritic arms of medium to thin thickness. This distinction is detailed in Figure 3*C*. The apical regions have significantly more spines per length of the dendrite (142.2 ± 17.8 spines/mm; mean ± SEM) than the proximal (78.8 ± 8.7 spines/mm; mean ± SEM) or medial (84.5 ± 9.0 spines/mm; mean ± SEM) regions (Kruskal–Wallis = 28.87, $p < 0.0001$; $n = 119$ dendrites; proximal vs apical: Kolmogorov–Smirnov $D = 0.47$, $p = 0.0008$; $n = 119$ dendrites; proximal vs medial: Kolmogorov–Smirnov $D = 0.19$, $p = 0.41$; $n = 119$ dendrites). However, in the *Cdh13* mutants, the relatively higher spine density in apical regions was absent, with all three regions having the same overall spine density [proximal: 36.4 ± 9.0 spines/mm (mean ± SEM); medial: 42.4 ± 9.4 spines/mm (mean ± SEM); apical: 33.8 ± 5.5 spines/mm (mean ± SEM); Kruskal–Wallis = 2.49, $p = 0.29$; $n = 49$ dendrites; proximal vs apical: Kolmogorov–Smirnov $D = 0.29$, $p = 0.39$; $n = 49$ dendrites; proximal vs medial: Kolmogorov–Smirnov $D = 0.33$, $p = 0.60$; $n = 49$ dendrites; Fig. 4*E*]. All three regions experienced a decreased spine density, with the apical region observing the largest percent decrease. The distribution of mature spines also shows a consistent trend of decline, with a larger decrease in apical regions in the absence of Cdh13 (12.6 ± 3.1 spines/mm; mean ± SEM) when compared with the control (79.9 ± 6.4 spines/mm; mean ± SEM; Kolmogorov–Smirnov $D = 0.79$; $p < 0.0001$; $n = 108$ dendrites; Fig. 4*F*). Taken together, these results indicate that Cdh13-dependent mature spines are present throughout the dendrites of wide-field neurons, but there is a higher density of them in apical dendrites in the superficial SGS.

Cdh13 is necessary to maintain adult wide-field neuron spines

Given the robust Cdh13 expression in the adult SC, we examined whether sustained Cdh13 expression is necessary to maintain mature wide-field neuron spines. We developed an AAV-carrying shRNA targeting against Cdh13 (Fig. 5*A*) fused to a Cre-dependent mOrange2 fluorescent label. This means that when this virus is introduced to a Cre-expressing neuron, the neuron will have Cdh13 mRNA expression knocked down and be fluorescently labeled. We injected this Cre-dependent AAV2/8 into the adult *Ntsr1-GN209-Cre* superior colliculus to disrupt Cdh13-mRNA expression in wide-field neurons. Of the neurons that received the shRNA for Cdh13 knockdown (RFP positive cells), all cells did not express Cdh13 mRNA (Fig. 5*D*). In the littermates, the shRNA scramble control was injected into the SC under the same protocol. Of the infected RFP-expressing cells in the control, 98.67% of cells expressed Cdh13 mRNA (Fig. 5*E*). The percent that did not express Cdh13 mRNA may indicate minor leaky-ness of the virus.

Notably, AAV2/8s were not axonally taken up by RGC axons (Fig. 5*F*,*G*). The retinas of the *Ntsr1-GN209-Cre* SC injected mice were assessed for RFP expression: Cre-expressing RGCs were not infected with Cre-dependent RFP via retrograde labeling from SC injections (Fig. 5*F*,*G*). Therefore, the shRNA viral injections in the SC selectively perturbed Cdh13 expression in the SC but not the retina. Conversely, we showed that injection of the AAV2/8-shRNA-DIO-mOrange2 into the eye did not affect Cdh13 expression in the SC. The virus was injected unilaterally into the eye of vGlut2-Cre mice, which marked all RGCs (Fig. 5*H*; Tran et al., 2019). Cdh13 expression was analyzed between each SC hemisphere: the contralateral hemisphere had Cdh13 knockdown in the innervating RGCs (Fig. 5*I*, shown by mOrange2-labeled and RFP-stained innervating axons), while the ipsilateral hemisphere did not. However, we did not observe major changes in Cdh13-enriched neuron expression in terms of either neuron numbers or laminar locations in the superficial SC (Fig. 5*J*,*K*). These data suggested that presynaptic Cdh13 perturbation was highly specific to presynaptic RGCs and did not lead to postsynaptic Cdh13 perturbations in the sSC.

Because the mouse necessary in this experiment (*VGlut2-Cre*; Fig. 5*H–K*) labels all excitatory cells in both the retina and the superior colliculus, genetic isolation of wide-field cells is not possible, even if the mouse were mated to a second Cre line previously established for wide-field labeling (*Ntsr1-BAC-Cre* or *Cdh13-KI-CreER*). Therefore, a different method was employed to assess wide-field cell location and persistence. We previously established that 91.8 ± 2.3% of *Ntsr1-BAC-Cre* (*Ntsr1-GN209-Cre*) labeled wide-field cells express Cdh13 and is generally absent in other excitatory neurons throughout the superior colliculus (Fig. 2*J*). In addition, both *Ntsr1-BAC-Cre* wide-field cell bodies (Gale and Murphy, 2014) and Cdh13-enriched cell bodies are restricted to the lower SO (Fig. 3*B*). And even though 35.7 ± 1.7% of Cdh13-expressing cells in the SO are not represented in the *Ntsr1-BAC-Cre* line (Fig. 2*K*), all *Cdh13-Cre-ER* labeled cells have *Ntsr1-BAC-Cre* wide-field cell morphology, laminar location, and spine distribution (Fig. 3*C–G*). Therefore, Cdh13-mRNA enrichment in the lower SO is used as a proxy for wide-field cell whole population labeling when other genetic labeling options are unavailable.

The knockdown or control virus was injected in the *Ntsr1-GN209-Cre* adult mouse (P60). The spine densities along the wide-field neuron dendrites were then analyzed (Fig. 6*A*). In the knockdown condition, overall spine densities (28.8 ± 3.5 spines/mm; mean ± SEM) significantly decreased compared with those of controls (93.6 ± 2.4 spines/mm, mean ± SEM; Fig. 6*C*,*D*; Kolmogorov–Smirnov $D = 0.61$; $p < 0.0001$; $n = 104$ dendrites). The knockdown densities were notably comparable with Cdh13 null mutants (39.3 ± 5.1 spines/mm; mean ± SEM; Fig. 4*B*). This effect resulted in a significant decrease in all spine types, with the largest percent decrease in mushroom spines (Kolmogorov–Smirnov $D = 0.55$; $p < 0.0001$; $n = 104$ dendrites; Fig. 6*D*). In addition, like in the Cdh13 null, the difference in spine distribution along the dendrite favoring apical regions was abolished in the adult knockdown condition, with the control distribution having a significant difference between the three regions (Kruskal–Wallis = 12.78; $p = 0.0017$; $n = 49$ dendrites) but the difference being absent in the knockdown (Kruskal–Wallis =

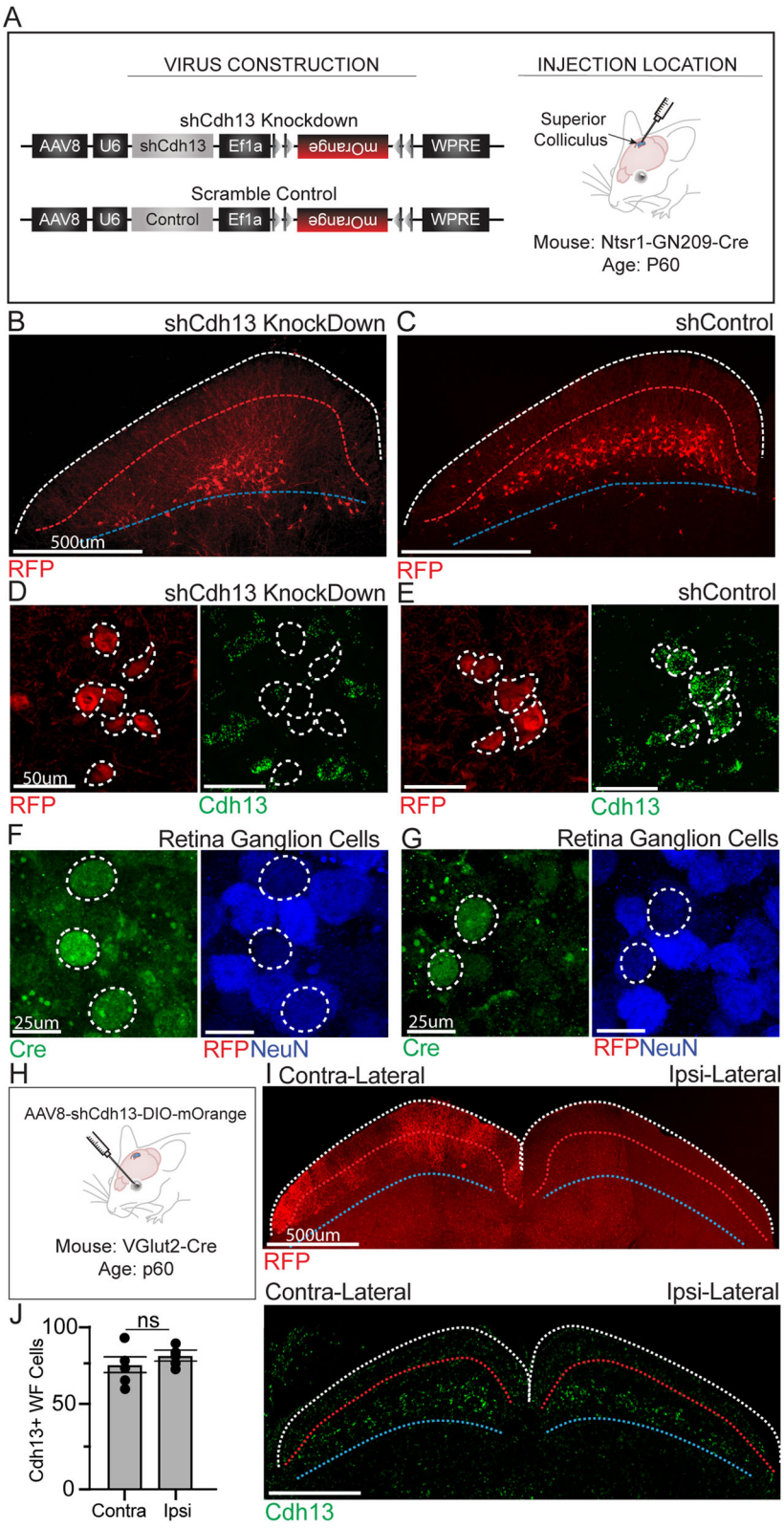

Figure 5. Virally mediated Cdh13 knockdown specifically eliminates Cdh13 expression. ***A***, Genetic scheme of viral *Cdh13* shRNA knockdown with Cre-dependent mOrange2 and the control counterpart. This virus is injected into the SC of a *Ntsr1-GN209-Cre* mouse at P60. ***B***, Confocal image confirming infection of wide-field neurons, specifically at the point of injection into the adult SC. AAV-U6-shCdh13-Ef1a-DIO-mOrange2 infected wide-field neurons and expressed mOrange2, amplified with RFP immunostaining. Scale bar, 500 µm. ***C***, Same conditions as ***B*** except the control virus is injected instead of the shCdh13. ***D***, Confocal image of virally infected wide-field neurons (RFP, left) to confirm *Cdh13* knockdown (Cdh13 mRNA green, right). White lines denote cell body boundaries. ***E***, Same conditions as ***D*** for the control virus. ***F***, Confocal image of whole-mount retina from the same *Ntsr1-GN209-Cre* in ***B*** and ***D*** showing Cre-expressing RGCs that are RFP negative. ***G***, Same conditions as ***F*** for the control virus. ***H***, Experimental diagram for retinal injection into *vGlut2-Cre* mouse. ***I***, *vGlut2-Cre* and AAV-mediate RGC axon labeling (RFP, red). Scale bar, 500 µm. ***J***, Comparisons between the contralateral and ipsilateral hemispheres in terms of Cdh13 expressing neurons in the sSC ($t = 0.78$; $p = 0.46$; $n = 5$ mice). ***K***, Sample image showing the Cdh13-expressing neurons in the sSC were not disrupted subject to the presynaptic (pan-RGC) knockdown of Cdh13. The brain slices came from the same brain as in Figure 5*H–J*, stained for Cdh13 in situ, to quantify Cdh13-expressing sSC neurons as a proxy for wide-field neurons (Fig. 2). Scale bar, 500 µm.

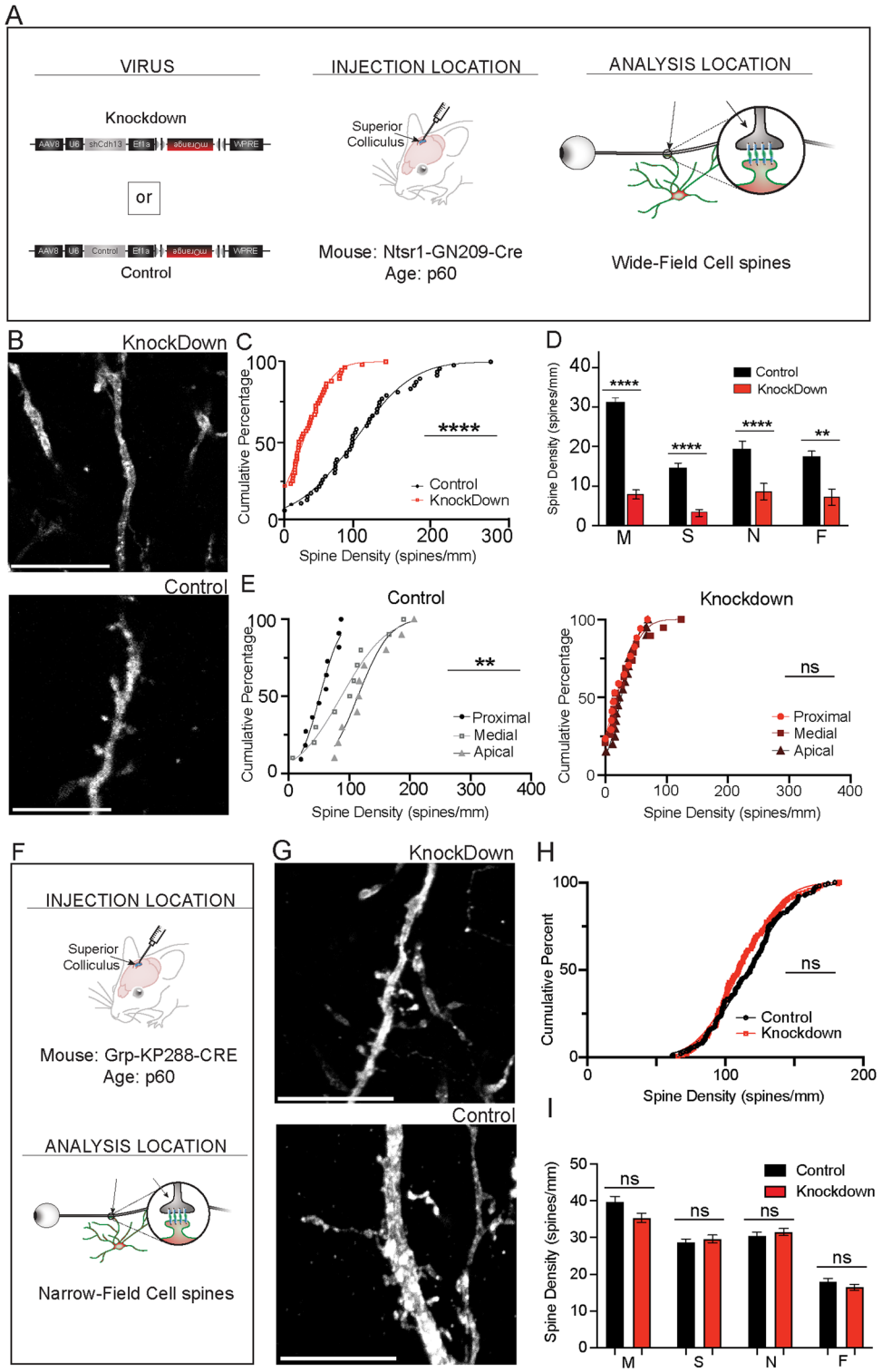

Figure 6. Adult Cdh13 expression is necessary for mature spine maintenance. ***A***, Illustration of experimental design and analysis location for Cdh13 knockdown in wide-field neurons. ***B***, Example images of dendritic spines of wide-field neurons with (top) *AAV-U6-shCdh13-Ef1a-DIO-mOrange2* or (bottom) *AAV8-shControl-DIO-mOrange2*. Scale bar, 5 µm. ***C***, Cumulative percentages of spine density comparison show decreases in spine density after adult Cdh13 shRNA knockdown (Kolmogorov–Smirnov $D = 0.61$; $p < 0.0001$; $n = 104$ dendrites). ***D***, Comparison of densities of different spine types, between *Ntsr1-GN209*-Cre control and knockdown. Mushroom (Kolmogorov–Smirnov $D = 0.55$; $p < 0.0001$; $n = 104$ dendrites), stubby (Kolmogorov–Smirnov $D = 0.44$; $p < 0.0001$; $n = 104$ dendrites), narrow (Kolmogorov–Smirnov $D = 0.56$; $p < 0.0001$; $n = 104$ dendrites), filopodia (Kolmogorov–Smirnov $D = 0.36$; $p = 0.0031$; $n = 104$ dendrites). ***E***, Comparison of cumulative percent distributions of overall spine densities at different locations along the dendrite from the cell body show a disproportionate decrease of spines in the apical regions in the knock-out (right; reds; Kruskal–Wallis = 0.81; $p = 0.87$; $n = 98$) compared with the control (left; blacks; Kruskal–Wallis = 12.78; $p = 0.0017$; $n = 49$ dendrites). ***F***, Illustration of experimental design and analysis location for Cdh13 knockdown in narrow-field cells. ***G***, Example images of dendritic spines of narrow-field cells with (top) *AAV-U6-shCdh13-Ef1a-DIO-mOrange2* or (bottom) *AAV-shRNA-Control-EF1a-DIO-mOrange2*. Scale bar, 5 µm. ***H***, Cumulative percentages of spine density comparison show no change in spine density after adult Cdh13 shRNA knockdown (Kolmogorov–Smirnov $D = 0.14$; $p = 0.11$; $n = 150$ dendrites). ***I***, Comparison of densities of different spine types between *Ntsr1-GN209*-Cre control and knockdown. Mushroom (Kolmogorov–Smirnov $D = 0.15$; $p = 0.059$; $n = 150$ dendrites), stubby (Kolmogorov–Smirnov $D = 0.08$; $p = 0.08$; $n = 150$ dendrites), narrow (Kolmogorov–Smirnov $D = 0.11$; $p = 0.36$; $n = 150$ dendrites), filopodia (Kolmogorov–Smirnov $D = 0.11$; $p = 0.36$; $n = 150$ dendrites). ns, $p > 0.05$, *$p < 0.05$, **$p < 0.01$, ***$p < 0.001$, ****$p < 0.0001$.

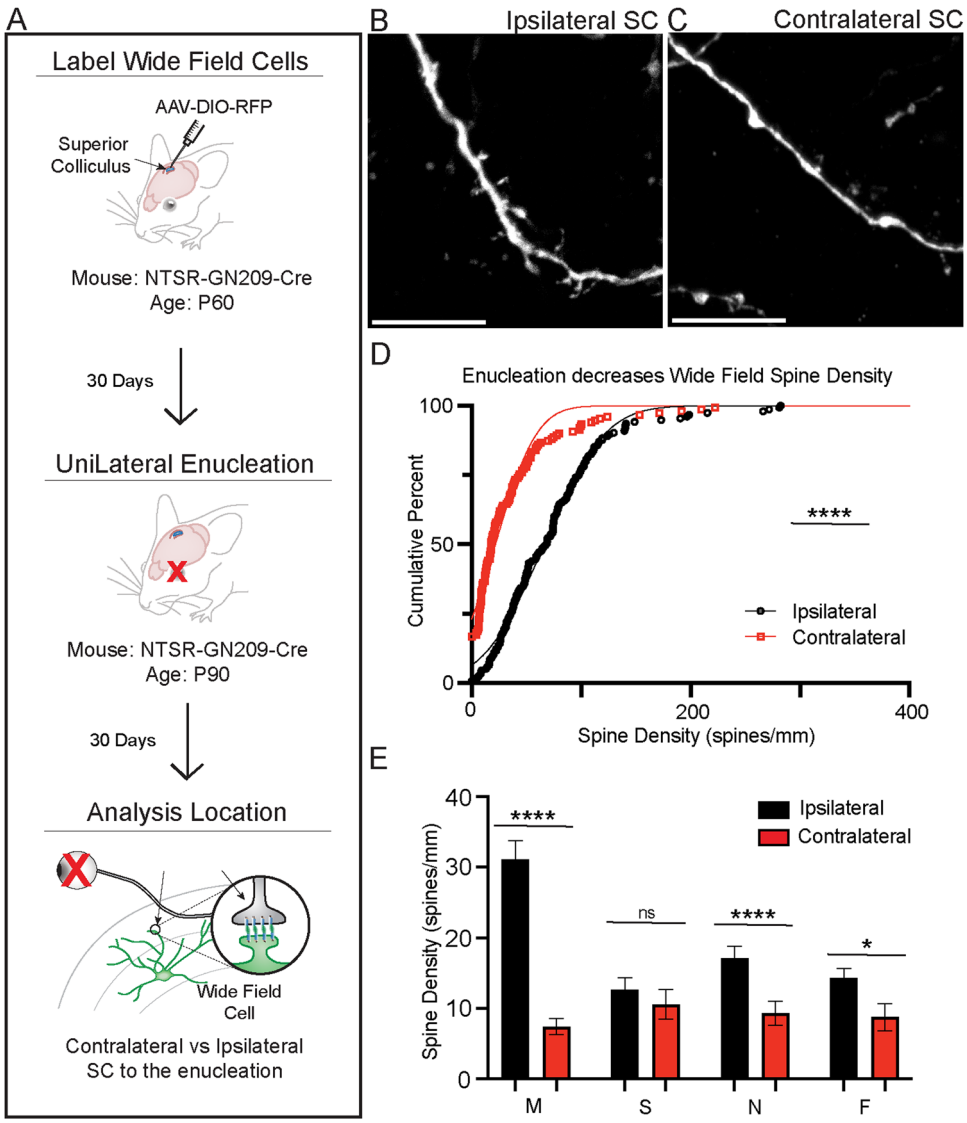

Figure 7. Adult eye enucleation unilaterally reduces wide-field neuron dendritic spines. ***A***, Illustration of experimental design for unilateral adult enucleation and subsequent analysis of wide-field neuron dendritic spines. ***B***, Example images of dendritic spines of wide-field neurons ipsilateral to the removed eye. Scale bar, 10 µm. ***C***, Example images of dendritic spines of wide-field neurons contralateral of the removed eye. Scale bar, 10 µm. ***D***, Comparison of cumulative percentages of spine densities between the ipsilateral (black control) and contralateral (red) SC hemispheres to the enucleated eye (Kolmogorov–Smirnov $D = 0.48$; $p < 0.0001$; $n = 150$ dendrites). ***E***, Comparison of densities of different spine types between *Ntsr1-GN209-Cre* control and knockdown. Mushroom (Kolmogorov–Smirnov $D = 0.42$; $p < 0.0001$; $n = 150$ dendrites), stubby (Kolmogorov–Smirnov $D = 0.25$; $p = 0.0001$; $n = 150$ dendrites), narrow (Kolmogorov–Smirnov $D = 0.29$; $p < 0.0001$; $n = 150$ dendrites), filopodia (Kolmogorov–Smirnov $D = 0.34$; $p < 0.00016$; $n = 150$ dendrites).

0.81; $p = 0.87$; $n = 98$; Fig. 6*E*). As additional proof, we introduced AAV-shRNA-mediated Cdh13 knockdown into narrow-field cells, similarly labeled in *Grp-KH288-Cre* as *Ntsr1-GN209-Cre* (Fig. 6*F*). Such an AAV-mediated shRNA Cdh13 knockdown did not lead to spine loss in narrow-field neurons (Kolmogorov–Smirnov $D = 0.14$; $p = 0.11$; $n = 150$ dendrites) or in any spine type [mushroom (Kolmogorov–Smirnov $D = 0.15$; $p = 0.059$; $n = 150$ dendrites), stubby (Kolmogorov–Smirnov $D = 0.08$; $p = 0.08$; $n = 150$ dendrites), narrow (Kolmogorov–Smirnov $D = 0.11$; $p = 0.36$; $n = 150$ dendrites), filopodia (Kolmogorov–Smirnov $D = 0.11$; $p = 0.36$; $n = 150$ dendrites); Fig. 6*G–I*].

Retina enucleation led to the spine decline of SC wide-field neurons

An important question is whether the Cdh13-dependent decrease in wide-field neuron spine density results from transsynaptic interaction between the retina and the superior colliculus. To test this hypothesis, we performed unilateral enucleations in adult *Ntsr1-GN2090-Cre* mice (Fig. 7*A*). Transgenic labeled wide-field neuron dendritic spines were assessed at 4 weeks post enucleations. In this case, wide-field neurons in the contralateral SC side were compared with the counterparts in ipsilateral SC as the control. The dendritic spine density was significantly reduced in the contralateral side, compared with that in ipsilateral controls (Kolmogorov–Smirnov $D = 0.48$; $p < 0.0001$; $n = 150$ dendrites; Fig. 7*B–D*). In addition, mushroom spine densities drastically decreased (Kolmogorov–Smirnov $D = 0.42$; $p < 0.0001$; $n = 150$ dendrites; Fig. 7*E*), compared with the other spine types [stubby (Kolmogorov–Smirnov $D = 0.25$; $p = 0.0001$; $n = 150$ dendrites), narrow (Kolmogorov–Smirnov $D = 0.29$; $p < 0.0001$; $n = 150$ dendrites), filopodia (Kolmogorov–Smirnov $D = 0.34$; $p < 0.00016$; $n = 150$ dendrites)]. These data demonstrated that presynaptic RGC axonal innervation is necessary to maintain wide-field neuron dendritic spines.

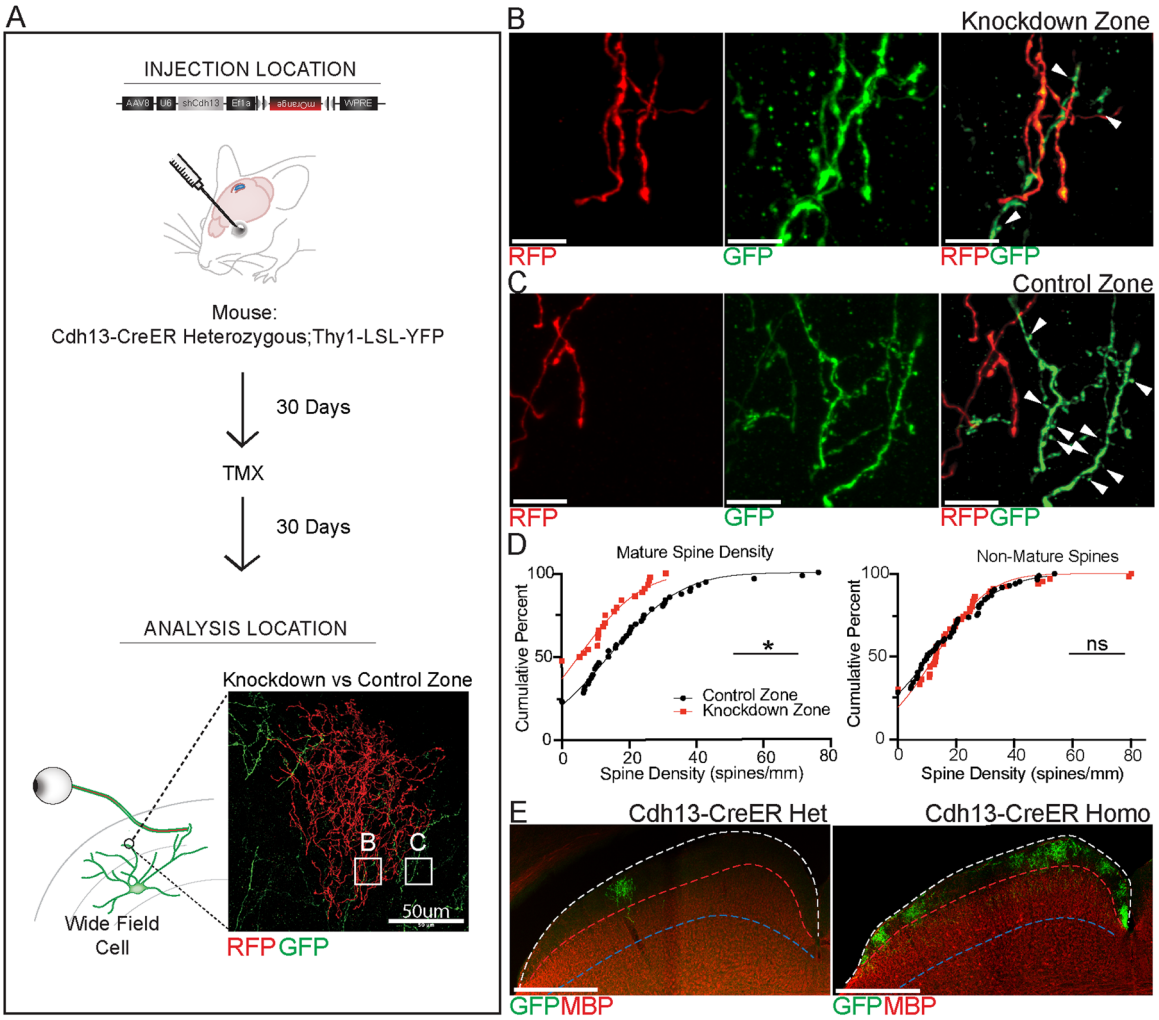

Figure 8. RGC-specific Cdh13-Knockdown locally reduces mature spines at the Cdh13-RGC axonal projection zone. ***A***, Illustration of experimental design for retinal Cdh13 knockdown in *Cdh13-CreER; Thy1-LSL-YFP15* heterozygous mouse. Analysis location examples are designated within the two white boxes (***B***,***C***). ***B***, Example confocal images of knockdown analysis zone within the *AAV2-U6-shRNA-Cdh13-EF1a-DIO-mOrange2* labeled RGC axon terminal in the SC. RFP (left) shows RGC labeled axons, GFP (middle) shows *Cdh13-CreER; Thy1-LSL-YFP15* labeled RGC axons, and WF dendrites. ***C***, Example confocal images of the control analysis zone outside the *AAV2-U6-shRNA-Cdh13-EF1a-DIO-mOrange2* labeled RGC axon terminal in the SC. RFP (left) shows RGC labeled axons, GFP (middle) shows *Cdh13-CreER; Thy1-LSL-YFP15* labeled RGC axons, and WF dendrites. Scale bar: ***B***, ***C***, 20 µm. ***D***, Cumulative percentage plots of spine densities of (left) mature mushroom spines (Kolmogorov–Smirnov $D = 0.29$; $p = 0.038$; $n = 100$ dendrites) and (right) non-mature spines (narrow, stubby/filopodia; Kolmogorov–Smirnov $D = 0.15$; $p = 0.39$; $n = 100$ dendrites). $n = 20$ mice, each data point is a dendrite. ***E***, Confocal images of Cdh13-RGC axon lamination in the SC for (left) heterozygous and (right) homozygous *Cdh13-CreER; Thy1-LSL-YFP15* mice. *AAV2-DIO-GFP* was injected into the eyes of these mice to label RGCs upon Tamoxifen administration exclusively. Scale bar, 500 µm.

Retinal Cdh13 knockdown reduces spine densities in postsynaptic wide-field neurons

Cdh13 recognition is homophilic (Ranscht and Bronner-Fraser, 1991; Vestal and Ranscht, 1992; Spranger et al., 2006; Ciatto et al., 2010). We hypothesized that presynaptic Cdh13 in RGCs is necessary for mature spine densities in wide-field neurons. To assess this, we delivered the same AAV carrying shRNA against Cdh13 into the retina of the *Cdh13-CreER; Thy1-LSL-YFP* line (Fig. 8*A*). After tamoxifen induction of Cre, Cdh13-expressing neurons in the retina and the SC will be labeled in YFP, and infected RGC neurons will express the *AAV-U6-shCdh13-Ef1a-DIO-mOrange2*. This allows for *Cdh13* knockdown and labeling in Cdh13-expressing RGCs without affecting Cdh13 expression in SC cells. Under these retinal knockdown conditions, we analyzed the postsynaptic spine densities of the wide-field neurons (Fig. 8*A*). We compared wide-field neuron spine densities within the area of RFP-expressing axonal terminals (Fig. 8*B*) with those outside the RFP-expressing axon terminals (Fig. 8*C*). Cdh13-expressing RGCs that have successful *AAV-U6-shCdh13-Ef1a-DIO-mOrange2* infection were labeled in both RFP (from the virus) and GFP (from the genetics of the mouse). Wide-field neurons and their dendrites are labeled in GFP from the genetics of the mouse line.

There is a general decrease in total WF spine density between the knockdown zones (56.6 ± 9.8 spines/mm; mean ± SEM) and the surrounding control areas (79.4 ± 10.9; mean ± SEM spines/mm; Kolmogorov–Smirnov $D = 0.23$, $p = 0.55$; $n = 100$ dendrites). However, a significant decrease in total mature spines was observed in the knockdown zones (8.5 ± 1.4 spines/mm; mean ± SEM) compared with the control zones (17.7 ± 2.3 spines/mm; mean ± SEM; Kolmogorov–Smirnov $D = 0.29$; $p = 0.038$; $n = 100$ dendrites; Fig. 8*D*). However, the densities of non-mature spines (stubby, narrow, and filopodia) remain unchanged (Kolmogorov–Smirnov $D = 0.15$; $p = 0.39$; $n = 100$ dendrites; Fig. 8*D*). We showed that shRNA for Cdh13 knockdown in RGCs did not affect Cdh13 expression in the SC (Fig. 5*I*,*J*). In

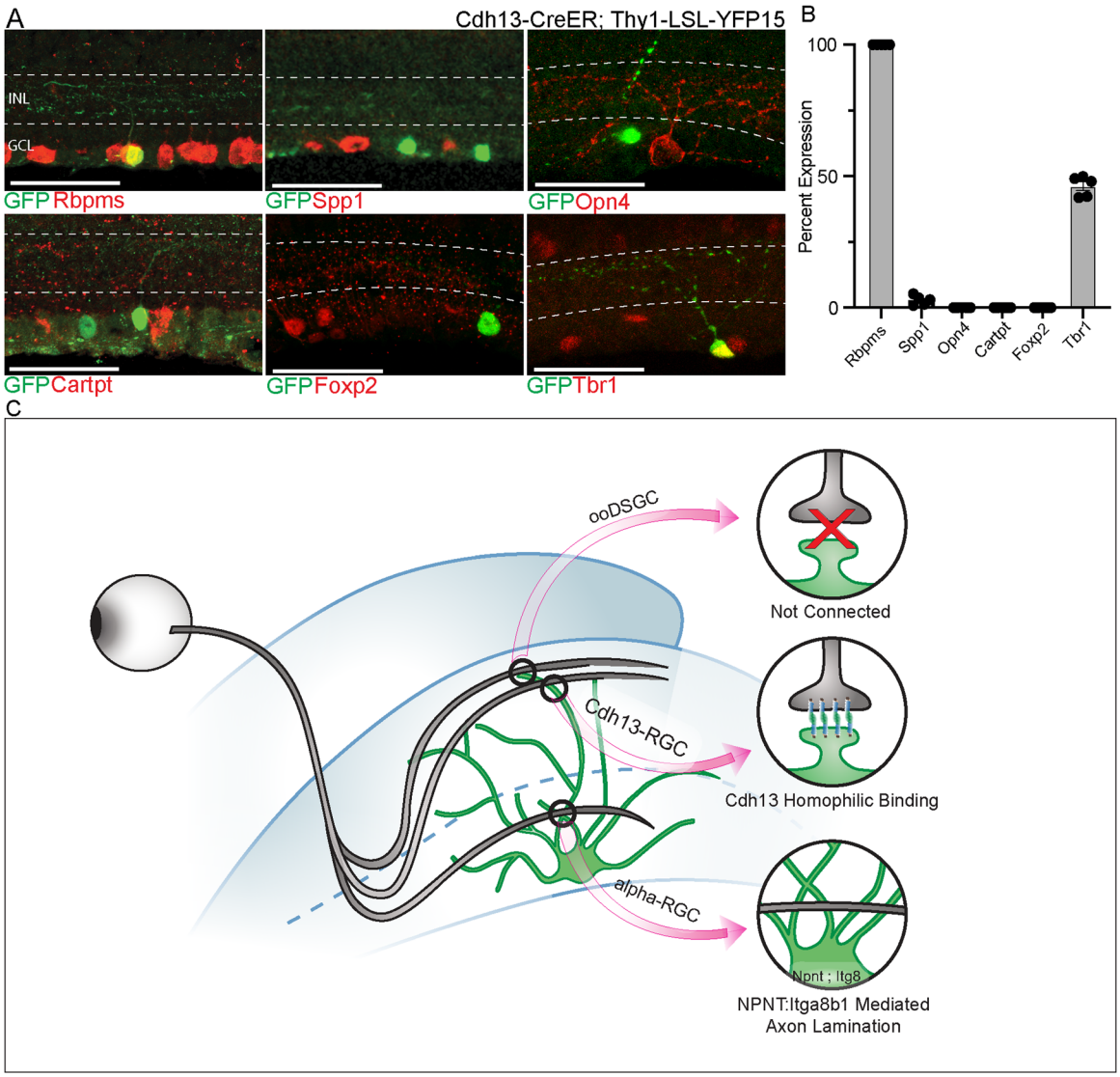

Figure 9. Immunohistochemistry markers for Cdh13-expressing RGCs. ***A***, Immunohistochemical stains for retinal proteins in *Cdh13-CreER; Thy1-LSL-YFP15* retinas. GFP labels Cdh13-RGCs. Scale bar, 50 µm. ***B***, Graphical quantification of (***A***). All expressed Rbpms; none of them expressed Opn4, Cartpt, or Foxp2; but 46.3 ± 1.7% expressed Tbr1; 2.9 ± 0.8% Spp1. $n = 5$ animals. ***C***, Graphical model: Cdh13 mediates a unique retinotectal synapse formation from presynaptic Cdh13-RGCs (not including αRGCs, ooDSGCs, ipRGCs) onto postsynaptic wide-field neurons, which mainly regulates spine formation. In contrast, Npnt-Itga8b1 mediates selective αRGCs synapse formation onto wide-field neurons, using a distinct mechanism. Notably, Cartpt-positive ooDSGCs do not form synapses onto wide-field neurons. Thus, the illustration summarized potential mechanisms mediating parallel retinotectal synapse formation.

addition, Cdh13-RGC axon lamination is not affected in Cdh13 knock-out animals (Fig. 8*E*). These results supported the idea that removing Cdh13 in RGCs reduces wide-field neurons' mature mushroom dendritic spine density exclusively within Cdh13-RGC axonal termination zones despite no disruption to Cdh13 expression in the wide-field neurons. Thus, presynaptic Cdh13 is necessary to maintain synaptic spine structures in the SC wide-field neurons. These data suggest that Cdh13 is a transsynaptic anchor that maintains mature spine structures within specific neuron types from the retina to the SC. Therefore, through its specific expression and transsynaptic mature spine maintenance in the retinotectal projection, Cdh13 directs neuron type-specific wiring between the retina and the SC.

To corroborate the results on SC neurons, we explored the identities of Cdh13-expressing RGCs. We utilized the same genetic reagents established above (*Cdh13-CreER; Thy1-LSL-YFP*) mouse line to visualize Cdh13-expressing retinal cells via tamoxifen injection. We characterized Cdh13 neurons in the retina using traditional immunohistochemistry based on a set of RGC subclass-specific markers (Zhao et al., 2023). We showed that all Cdh13-expressing retinal neurons were RGCs (Rbpms-positive). Among them, very few, if any of them, expressed Spp1, Cartpt, Opn4, or Foxp2; however, approximately half of them expressed Tbr1 (Fig. 9*A*,*B*). While detailed subtypes of Cdh13-RGCs remained determined, these data indicated that Cdh13-RGCs belong to a distinct subclass, different from αRGCs, ooDSGCs, ipRGCs, or F-RGCs. Thus, Cdh13-mediated retinotectal synapse formation is distinct from other parallel pathways for the other RGC types.

Discussion

Our current study explored the role of a homophilic Type II Cdh, Cdh13, in transneuronal synaptic maintenance. Our past work focused on Type II Cdhs' role in regulating anatomical and connectivity changes within the retina (Duan et al., 2014, 2018). Our

current work expanded the expression survey to the retinotectal synapses, and the combinatorial expression suggested a general role of Type II Cdhs in cell type-directed synaptic assembly in the CNS. Particularly, our current study put Cdh13, one Type II Cdh, in the neuron–neuron connectivity setting and revealed how specific neural circuits from the retina to the brain may utilize specific Cdhs for synapse maintenance. We showed a uniquely enriched Cdh13 expression in wide-field neurons. Global Cdh13 mutants led to a reduction of mature dendritic spine density, specifically in apical regions. AAV-mediated Cdh13 elimination in the adult retina, or SC, led to a similar reduction of wide-field neuron dendritic spine density. Identifying Cdh-directed circuit pairs from the retina to the SC can further understand how visual inputs are relayed to inform behavioral outputs. Taken together, Cdh13's restricted expression in RGC and SC subsets allows for cell type-specific transneuronal recognition.

One of the major findings of the current study is about the dendritic spine changes within the wide-field neurons within the sSC. Dendritic spines are the primary site of glutamatergic input in the CNS, and their reduction has been shown to affect synaptic function negatively (Boros et al., 2017, 2019; Walker et al., 2021). For retinotectal connectivity, glutamatergic input is extremely important as RGCs are glutamatergic. In excitatory neurons, most glutamatergic synapses are made on the heads of dendritic spines, each of which houses the postsynaptic terminal of a single glutamatergic synapse (Alvarez et al., 2007). Our current data are primarily acquired in the young adult SC, where the dendritic spines are well formed. Thus, our current study provides evidence that Cdh13 is essential to maintaining dendritic spines. However, we cannot rule out the possibility that Cdh13 plays an equally important role in synapse formation (Fig. 5*E*). Cdh13 is a GPI-coupled Type II cadherin involved in CNS axonal targeting and synaptic regulation (Philippova et al., 2008; Ciatto et al., 2010; Kiser et al., 2019; Nguyen et al., 2020). Cdh13 resides in lipid rafts, concentrating on synapse-related proteins (Ranscht and Dours-Zimmermann, 1991; Hering et al., 2003; Philippova et al., 2008). Cdh13 would then bind homophilically with the transsynaptic cell to anchor the structures in place, with the intracellular event largely undefined. In other words, the current study indicated that the cell–cell recognition but not the downstream signaling events may lead to specific retinotectal synapse changes.

Notably, past studies, including ours, identified Npnt, a secreted extracellular matrix molecule in facilitating the synaptic choices from presynaptic retinal neurons with wide-field neurons during postnatal development (Su et al., 2021; Tsai et al., 2022). We demonstrated a selective role for Npnt-Itg8 signaling in mediating synaptic recognition between αRGCs and wide-field neurons. We also found that postsynaptic Npnt patterned the axonal targeting and restriction of αRGCs to the appropriate SO lamina from wide-field neurons. Additionally, in the current study, we showed that Cdh13-mediated RGC and wide-field neuron connections did not impact the laminar restriction of Cdh13-RGC axons (Figs. 7, 8). Although Cdh13 and Npnt signals act on wide-field neurons, they each have distinct functions in directing connectivity between different RGC types onto wide-field neurons. Thus, each retinotectal pathway may utilize a distinct signaling mechanism for synaptic specificity (Fig. 9*C*).

Cdh13-CreER primarily labels wide-field neurons, which were also labeled independently by *Ntsr1-GN209-Cre line* (Gale and Murphy, 2014), *Cbln2-GFP* line (Seigneur and Sudhof, 2017; Xie et al., 2021), and *Npnt-Flp* line (Tsai et al., 2022), sharing similar morphologies and laminations. Functionally, wide-field neurons are tuned to slow-moving, small stimuli over a large receptive field (Gale and Murphy, 2014) and project to the lateral posterior nucleus of the thalamus (LP; Dhande and Huberman, 2014; Gale and Murphy, 2014; Brenner et al., 2023). Thus, physiological, functional, and behavioral consequences of Cdh13 mutants remain to be explored based on the morphological study of wide-field neurons in retinotectal synapse maintenance and circuit assembly.

References

Alvarez VA, Ridenour DA, Sabatini BL (2007) Distinct structural and ionotropic roles of NMDA receptors in controlling spine and synapse stability. J Neurosci 27:7365–7376.

Basu R, et al. (2017) Heterophilic type II cadherins are required for high-magnitude synaptic potentiation in the hippocampus. Neuron 96:160–176.e8.

Ben Fredj N, Hammond S, Otsuna H, Chien CB, Burrone J, Meyer MP (2010) Synaptic activity and activity-dependent competition regulates axon arbor maturation, growth arrest, and territory in the retinotectal projection. J Neurosci 30:10939–10951.

Benson DL, Tanaka H (1998) N-cadherin redistribution during synaptogenesis in hippocampal neurons. J Neurosci 18:6892–6904.

Boros BD, Greathouse KM, Gentry EG, Curtis KA, Birchall EL, Gearing M, Herskowitz JH (2017) Dendritic spines provide cognitive resilience against Alzheimer's disease. Ann Neurol 82:602–614.

Boros BD, Greathouse KM, Gearing M, Herskowitz JH (2019) Dendritic spine remodeling accompanies Alzheimer's disease pathology and genetic susceptibility in cognitively normal aging. Neurobiol Aging 73:92–103.

Bozdagi O, Shan W, Tanaka H, Benson DL, Huntley GW (2000) Increasing numbers of synaptic puncta during late-phase LTP: n-cadherin is synthesized, recruited to synaptic sites, and required for potentiation. Neuron 28:245–259.

Brenner JM, Beltramo R, Scanziani M (2023) A genetically defined tecto-thalamic pathway drives a system of superior-colliculus-dependent visual cortices. Neuron 111:2247–2257.e7.

Buffelli M, Burgess RW, Feng G, Lobe CG, Lichtman JW, Sanes JR (2003) Genetic evidence that relative synaptic efficacy biases the outcome of synaptic competition. Nature 424:430–434.

Byun H, Kwon S, Ahn HJ, Liu H, Forrest D, Demb JB, Kim IJ (2016) Molecular features distinguish ten neuronal types in the mouse superficial superior colliculus. J Comp Neurol 524:2300–2321.

Cang J, Savier E, Barchini J, Liu X (2018) Visual function, organization, and development of the mouse superior colliculus. Annu Rev Vis Sci 4:239–262.

Cheng TW, Liu XB, Faulkner RL, Stephan AH, Barres BA, Huberman AD, Cheng HJ (2010) Emergence of lamina-specific retinal ganglion cell connectivity by axon arbor retraction and synapse elimination. J Neurosci 30:16376–16382.

Ciatto C, et al. (2010) T-cadherin structures reveal a novel adhesive binding mechanism. Nat Struct Mol Biol 17:339–347.

Dewitz C, Duan X, Zampieri N (2019) Organization of motor pools depends on the combined function of N-cadherin and type II cadherins. Development 146:dev180422.

Dhande OS, Huberman AD (2014) Retinal ganglion cell maps in the brain: implications for visual processing. Curr Opin Neurobiol 24:133–142.

Duan X, et al. (2007) Disrupted-in-schizophrenia 1 regulates integration of newly generated neurons in the adult brain. Cell 130:1146–1158.

Duan X, Krishnaswamy A, De la Huerta I, Sanes JR (2014) Type II cadherins guide assembly of a direction-selective retinal circuit. Cell 158:793–807.

Duan X, Qiao M, Bei F, Kim IJ, He Z, Sanes JR (2015) Subtype-specific regeneration of retinal ganglion cells following axotomy: effects of osteopontin and mTOR signaling. Neuron 85:1244–1256.

Duan X, Krishnaswamy A, Laboulaye MA, Liu J, Peng YR, Yamagata M, Toma K, Sanes JR (2018) Cadherin combinations recruit dendrites of distinct retinal neurons to a shared interneuronal scaffold. Neuron 99:1145–1154.e6.

Fannon AM, Colman DR (1996) A model for central synaptic junctional complex formation based on the differential adhesive specificities of the cadherins. Neuron 17:423–434.

Fredette BJ, Miller J, Ranscht B (1996) Inhibition of motor axon growth by T-cadherin substrata. Development 122:3163–3171.
Gale SD, Murphy GJ (2014) Distinct representation and distribution of visual information by specific cell types in mouse superficial superior colliculus. J Neurosci 34:13458–13471.
Gale SD, Murphy GJ (2018) Distinct cell types in the superficial superior colliculus project to the dorsal lateral geniculate and lateral posterior thalamic nuclei. J Neurophysiol 120:1286–1292.
Graham HK, Duan X (2021) Molecular mechanisms regulating synaptic specificity and retinal circuit formation. Wiley Interdiscip Rev Dev Biol 10: e379.
Hayashi Y, Majewska AK (2005) Dendritic spine geometry: functional implication and regulation. Neuron 46:529–532.
Hering H, Lin CC, Sheng M (2003) Lipid rafts in the maintenance of synapses, dendritic spines, and surface AMPA receptor stability. J Neurosci 23: 3262–3271.
Hirano S, Takeichi M (2012) Cadherins in brain morphogenesis and wiring. Physiol Rev 92:597–634.
Hong YK, Kim IJ, Sanes JR (2011) Stereotyped axonal arbors of retinal ganglion cell subsets in the mouse superior colliculus. J Comp Neurol 519: 1691–1711.
Huberman AD, Manu M, Koch SM, Susman MW, Lutz AB, Ullian EM, Barres BA (2008) Architecture and activity-mediated refinement of axonal projections from a mosaic of genetically identified retinal ganglion cells. Neuron 59:425–438.
Huntley GW, Benson DL (1999) Neural (N)-cadherin at developing thalamocortical synapses provides an adhesion mechanism for the formation of somatopically organized connections. J Comp Neurol 407:453–471.
Killen AC, Barber M, Paulin JJW, Ranscht B, Parnavelas JG, Andrews WD (2017) Protective role of cadherin 13 in interneuron development. Brain Struct Funct 222:3567–3585.
Kim IJ, Zhang Y, Meister M, Sanes JR (2010) Laminar restriction of retinal ganglion cell dendrites and axons: subtype-specific developmental patterns revealed with transgenic markers. J Neurosci 30:1452–1462.
Kiser DP, Popp S, Schmitt-Bohrer AG, Strekalova T, van den Hove DL, Lesch KP, Rivero O (2019) Early-life stress impairs developmental programming in cadherin 13 (CDH13)-deficient mice. Prog Neuropsychopharmacol Biol Psychiatry 89:158–168.
Lehto MT, Sharom FJ (1998) Release of the glycosylphosphatidylinositol-anchored enzyme ecto-5'-nucleotidase by phospholipase C: catalytic activation and modulation by the lipid bilayer. Biochem J 332:101–109.
Manabe T, Togashi H, Uchida N, Suzuki SC, Hayakawa Y, Yamamoto M, Yoda H, Miyakawa T, Takeichi M, Chisaka O (2000) Loss of cadherin-11 adhesion receptor enhances plastic changes in hippocampal synapses and modifies behavioral responses. Mol Cell Neurosci 15:534–546.
Missaire M, Hindges R (2015) The role of cell adhesion molecules in visual circuit formation: from neurite outgrowth to maps and synaptic specificity. Dev Neurobiol 75:569–583.
Molenaar A (1992) Aesthetic surgery on psychologically disturbed patients. Plast Reconstr Surg 89:1173–1175.
Nguyen PT, et al. (2020) Microglial remodeling of the extracellular matrix promotes synapse plasticity. Cell 182:388–403.e15.
O'Leary DD, McLaughlin T (2005) Mechanisms of retinotopic map development: Ephs, ephrins, and spontaneous correlated retinal activity. Prog Brain Res 147:43–65.
Oliveira AF, Yonehara K (2018) The mouse superior colliculus as a model system for investigating cell type-based mechanisms of visual motor transformation. Front Neural Circuits 12:59.
Philippova M, Ivanov D, Joshi MB, Kyriakakis E, Rupp K, Afonyushkin T, Bochkov V, Erne P, Resink TJ (2008) Identification of proteins associating with glycosylphosphatidylinositol- anchored T-cadherin on the surface of vascular endothelial cells: role for Grp78/BiP in T-cadherin-dependent cell survival. Mol Cell Biol 28:4004–4017.
Poliak S, Norovich AL, Yamagata M, Sanes JR, Jessell TM (2016) Muscle-type identity of proprioceptors specified by spatially restricted signals from limb mesenchyme. Cell 164:512–525.
Ranscht B, Bronner-Fraser M (1991) T-cadherin expression alternates with migrating neural crest cells in the trunk of the avian embryo. Development 111:15–22.
Ranscht B, Dours-Zimmermann MT (1991) T-cadherin, a novel cadherin cell adhesion molecule in the nervous system lacks the conserved cytoplasmic region. Neuron 7:391–402.
Sanes JR, Masland RH (2015) The types of retinal ganglion cells: current status and implications for neuronal classification. Annu Rev Neurosci 38:221–246.
Sanes JR, Yamagata M (2009) Many paths to synaptic specificity. Annu Rev Cell Dev Biol 25:161–195.
Seigneur E, Sudhof TC (2017) Cerebellins are differentially expressed in selective subsets of neurons throughout the brain. J Comp Neurol 525: 3286–3311.
Spranger J, Verma S, Gohring I, Bobbert T, Seifert J, Sindler AL, Pfeiffer A, Banks WA (2006) Adiponectin does not cross the blood-brain barrier but modifies cytokine expression of brain endothelial cells. Diabetes 55: 141–147.
Su J, Sabbagh U, Liang Y, Olejnikova L, Dixon KG, Russell AL, Chen J, Pan YA, Triplett JW, Fox MA (2021) A cell-ECM mechanism for connecting the ipsilateral eye to the brain. Proc Natl Acad Sci U S A 118:e2104343118.
Suzuki SC, Furue H, Koga K, Jiang N, Nohmi M, Shimazaki Y, Katoh-Fukui Y, Yokoyama M, Yoshimura M, Takeichi M (2007) Cadherin-8 is required for the first relay synapses to receive functional inputs from primary sensory afferents for cold sensation. J Neurosci 27:3466–3476.
Tanaka H, Shan W, Phillips GR, Arndt K, Bozdagi O, Shapiro L, Huntley GW, Benson DL, Colman DR (2000) Molecular modification of N-cadherin in response to synaptic activity. Neuron 25:93–107.
Tang L, Hung CP, Schuman EM (1998) A role for the cadherin family of cell adhesion molecules in hippocampal long-term potentiation. Neuron 20: 1165–1175.
Tanihara H, Sano K, Heimark RL, St John T, Suzuki S (1994) Cloning of five human cadherins clarifies characteristic features of cadherin extracellular domain and provides further evidence for two structurally different types of cadherin. Cell Adhes Commun 2:15–26.
Tran NM, et al. (2019) Single-cell profiles of retinal ganglion cells differing in resilience to injury reveal neuroprotective genes. Neuron 104:1039–1055.e12.
Tsai NY, et al. (2022) Trans-seq maps a selective mammalian retinotectal synapse instructed by nephronectin. Nat Neurosci 25:659–674.
Uchida N, Honjo Y, Johnson KR, Wheelock MJ, Takeichi M (1996) The catenin/cadherin adhesion system is localized in synaptic junctions bordering transmitter release zones. J Cell Biol 135:767–779.
Vagnozzi AN, et al. (2022) Coordinated cadherin functions sculpt respiratory motor circuit connectivity. Elife 11:e82116.
Vestal DJ, Ranscht B (1992) Glycosyl phosphatidylinositol–anchored T-cadherin mediates calcium-dependent, homophilic cell adhesion. J Cell Biol 119:451–461.
Walker CK, Greathouse KM, Boros BD, Poovey EH, Clearman KR, Ramdas R, Muhammad HM, Herskowitz JH (2021) Dendritic spine remodeling and synaptic tau levels in PS19 tauopathy mice. Neuroscience 455:195–211.
Xie Z, et al. (2021) Transcriptomic encoding of sensorimotor transformation in the midbrain. Elife 10:e69825.
Yamagata M, Herman JP, Sanes JR (1995) Lamina-specific expression of adhesion molecules in developing chick optic tectum. J Neurosci 15:4556–4571.
Yamagata M, Duan X, Sanes JR (2018) Cadherins interact with synaptic organizers to promote synaptic differentiation. Front Mol Neurosci 11:142.
Yogev S, Shen K (2014) Cellular and molecular mechanisms of synaptic specificity. Annu Rev Cell Dev Biol 30:417–437.
Zhao C, Teng EM, Summers RG Jr, Ming GL, Gage FH (2006) Distinct morphological stages of dentate granule neuron maturation in the adult mouse hippocampus. J Neurosci 26:3–11.
Zhao M, et al. (2023) Osteopontin drives retinal ganglion cell resiliency in glaucomatous optic neuropathy. Cell Rep 42:113038.
Zito K, Svoboda K (2002) Activity-dependent synaptogenesis in the adult mammalian cortex. Neuron 35:1015–1017.